Materials Science & Engineering A 948 (2025) 149375

Contents lists available at ScienceDirect

Materials Science & Engineering A

journal homepage: www.elsevier.com/locate/msea

Achieving 1.2 GPa tensile strength in Cu–15Ni–8Sn alloy via large-strain rotary swaging: Multi-scale microstructure evolution and strengthening mechanisms

Shaodan Yang [a,b,c], Yanjun Zhou [c,d,e,*], Haoran Wu [a,c,**], Yunqi Shan [a,c], Chenyang Ge [a,b,c], Juan Du [a,c], Lei Zhao [a,c], Ran Yang [f], Zhiyuan Zhu [a], Xu Gao [a,c], Weiyang Long [a,b,c], Kai Sun [a,b,c], Yonghao Zhao [a,g,h,***], Kexing Song [a,b,c,****]

[a] Institute of Materials, Henan Academy of Sciences, Zhengzhou, 450002, China
[b] School of Material Science & Engineering, Zhengzhou University, Zhengzhou, 450001, China
[c] Henan Key Laboratory of Advanced Conductor Materials, Zhengzhou, 450002, China
[d] School of Material Science and Engineering, Henan University of Science and Technology, Luoyang, 471023, China
[e] Chinalco Luoyang Copper Processing Co., Ltd., Luoyang, 471003, China
[f] School of Medical Technology and Engineering, Henan University of Science and Technology, China
[g] Jiangsu Provincial Engineering Research Center for Structure-Function Integrated Metallic Materials for Harsh Environments, College of Materials Science and Engineering, Hohai University, Changzhou, 213200, China
[h] Innovation Center for Critical Materials in Hydraulic Infrastructure Safety and Water Environment Restoration, College of Materials Science and Engineering, Hohai University, Changzhou, 213200, China

ARTICLE INFO

Keywords:
Cu–15Ni–8Sn alloy
Large-strain rotary swaging
Nanotwins
Nanocrystal
Strengthening mechanism

ABSTRACT

The Cu–15Ni–8Sn alloy is characterized by high strength and excellent wear and corrosion resistance. As service conditions for critical components in aerospace, oil and gas extraction, and other fields become increasingly demanding, the pursuit of its ultimate strength has become more urgent. In this paper, the effects of different strains ($\varepsilon = 0$–3.9) on the hardness, strength, and characteristic microstructural such as dislocations and twins of Cu–15Ni–8Sn alloy after rotary swaging were systematically studied. The evolution of typical microstructure characteristic nodes in Cu–15Ni–8Sn alloy under the large-strain rotary swaging is proved: Dislocation → Cross twins ($\varepsilon \geq 1.3$) → Layered fine grains ($\varepsilon \geq 1.8$) → Nanotwins ($\varepsilon \geq 2.2$) → Nanocrystals ($\varepsilon \geq 3.2$). It is revealed that after rotary swaging at large-strain ($\varepsilon = 3.9$), the whole alloy matrix exhibits the high-density dislocations and layered fine grains, while nanotwins and nanocrystals establishes locally. The ultra-high strength of the rotary swagged alloy at $\varepsilon = 3.9$ is attributed to ultra-high denser dislocation (6.97×10^{15} m^{-2}) and refined grain (1.23 μm). When the accumulative strain $\varepsilon = 3.9$, the tensile strength and yield strength are 1200 MPa and 1156 MPa, which are 1.58 times and 3.22 times higher than those of the undeformed state ($\varepsilon = 0$), respectively. This result proves the feasibility of accumulating large deformation and thus significant strength limit of Cu-15Ni-8Sn alloy by single-step cold rotary swaging. It lays a theoretical foundation for the development and application of this alloy in demanding service conditions across multiple scenarios.

1. Introduction

The Cu–15Ni–8Sn alloy is a promising alternative to beryllium copper alloys owing to its high strength, high elasticity, excellent wear and corrosion resistances [1–4]. In addition, high strength Cu–15Ni–8Sn alloys must be fabricated to meet the stringent performance

* Corresponding authors. Henan Key Laboratory of Advanced Conductor Materials, Zhengzhou, 450002, China.
** Corresponding author. Institute of Materials, Henan Academy of Sciences, Zhengzhou, 450002, China.
*** Corresponding authors. Institute of Materials, Henan Academy of Sciences, Zhengzhou, 450002, China.
**** Corresponding author. Institute of Materials, Henan Academy of Sciences, Zhengzhou, 450002, China.
E-mail addresses: dazhou456@163.com (Y. Zhou), haoranwuted@163.com (H. Wu), yhzhao@njust.edu.cn (Y. Zhao), kxsong@haust.edu.cn (K. Song).

https://doi.org/10.1016/j.msea.2025.149375
Received 24 July 2025; Received in revised form 29 October 2025; Accepted 30 October 2025
Available online 1 November 2025

Table 1
Chemical composition of the Cu–15Ni–8Sn alloys.

Alloys	wt./%		
	Ni	Sn	Cu
Cu–15Ni–8Sn	15.34	8.16	balance

requirements of key components used in aerospace, marine engineering, oil and gas exploitation, and heavy-duty machinery [5–7].

During the research and development of this alloy, researchers commonly apply cold deformation processes such as rolling or drawing before aging of the Cu–15Ni–8Sn alloy to enhance its strength, with proven effectiveness [8–11]. For instance, Zhongkai Guo et al. applied rolling reductions of 50 %, 70 %, and 90 % to the solution-treated Cu–15Ni–8Sn alloy, resulting in increased tensile strengths of 701 MPa, 827 MPa, and 905 MPa, respectively. For the rolling deformation, high-density dislocations are formed in the alloy matrix, and the grains are significantly refined. High-density dislocations were formed within the alloy matrix during rolling deformation, and the grains were significantly refined. However, the number of deformation twins in the alloy is still very small even if the cumulative deformation is as high as 90 % [8]. Kaixuan Jiang et al. investigated the effects of cold-drawing deformation at 30 %, 50 %, and 70 % on the microstructure and properties of the Cu–15Ni–8Sn alloy, revealing that its tensile strength reached 972 MPa at 70 % deformation. However, due to the work hardening effect, it is difficult to further realize large cold deformation by drawing process, which also restricts the further improvement of strength [9]. Although these research methods enhance the tensile strength of Cu-15Ni-8Sn alloy, they also show the limitations of traditional plastic deformation processes such as drawing and rolling in further strength enhancement. Specifically, due to inherent limitations in their applied strain rates and stress states, these processes lack the necessary driving force or energetic conditions to effectively activate deformation mechanisms such as twinning or to promote substantial microstructural refinement. In addition, relevant scholars have found that through cold drawing deformation with large strains, a large number of nano-twin structures can be formed in the copper matrix, thereby greatly improving the strength of copper alloys. For example, Yanbin Jiang et al. prepared Cu-9Ni-6Sn alloy bars with axial columnar crystals with a diameter of 10.5 mm by directional solidification technique and directly cold-drawn to 40 μm ultrafine wires. The Cu-9Ni-6Sn alloy underwent cold drawing with a high train of 11.23 and obtained an average grain size of ~38 nm, which exhibited a tensile strength of 1453 MPa. In the final stage of continuous cold processing, the fine detwinning grains persist in deforming along the axial direction, culminating in the development of fibrous structures. This ultimately imparts the alloy with remarkable strength [12]. Heung Nam Han et al. prepared a Cu-Ni-Si-Ti alloy with a large number of nano-twin structures by cold drawing with 95 % deformation, achieving a synergistic improvement of high strength (1050 MPa) and high conductivity (43 %IACS). The strengthening mechanism of this alloy is mainly through the formation of a large number of nano-sized Ni_2Si precipitates and nano-twins in the copper matrix after cold deformation with large strain, which significantly increases its strength [13]. Yinfei Ju et al. found that the Cu-12Sn-2Ni alloy wire reached a tensile strength of 1.3 GPa through a cold drawing process without intermediate annealing (the cumulative deformation reached 97 %). Through cold deformation at high strains, the grains are refined into nanofiber structures and dense deformation twins are formed. In addition, the low stacking faults of the alloy can promote a significant increase in dislocation density, and then achieve ultra-high strength through dislocation strengthening and grain boundary strengthening [14]. The above research results and the mechanism analysis of the strength greatly improved by cold drawing can provide reference for the research work of this paper.

In contrast, rotary swaging is a typical severe plastic deformation (SPD) process and a near-net-shape forming technology. Due to the characteristics of high strain rate, large cumulative strain, and multi-directional compression deformation, rotary swaging can effectively accumulate dislocations and grain boundary defects as well as activate multiple slip systems and twin deformation [15–21]. These characteristics make rotary swaging an effective method to realize the deep refinement of microstructure and further enhance the strength of copper alloys. Kaixuan Zhou et al. employed rotary swaging (equivalent strain $\varepsilon = 2.5$) to prepare Cu–Al alloy rods with hard nanocrystalline (NC) core

Table 2
Rotary swaging passes and cumulative strain of solution-treated Cu–15Ni–8Sn alloy at room temperature.

Rotary swaging pass	Diameter after rotary swaging (mm)	Equivalent strain
0	30.0	0.0
1	27.0	0.2
2	24.0	0.4
3	21.0	0.7
4	18.0	1.0
5	16.0	1.3
6	13.9	1.5
7	13.0	1.7
8	12.4	1.8
9	11.3	2.0
10	10.0	2.2
11	8.8	2.5
12	8.0	2.6
13	7.1	2.9
14	6.2	3.2
15	5.0	3.6
16	4.2	3.9

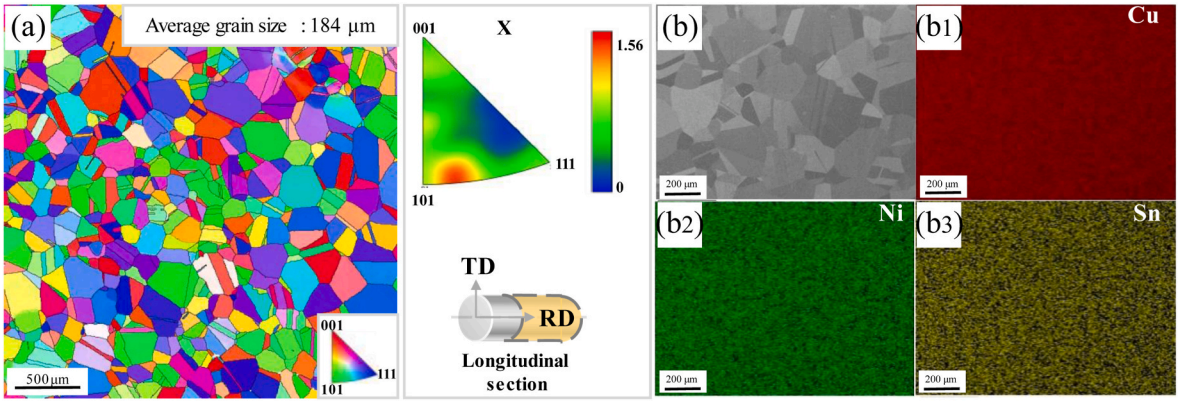

Fig. 1. SEM image and element plane distribution diagram of the Cu–15Ni–8Sn alloy after solution treatment. (a) SEM images; (b1-4) Partially enlarged view and the EDS elemental mapping of Cu, Ni, and Sn.

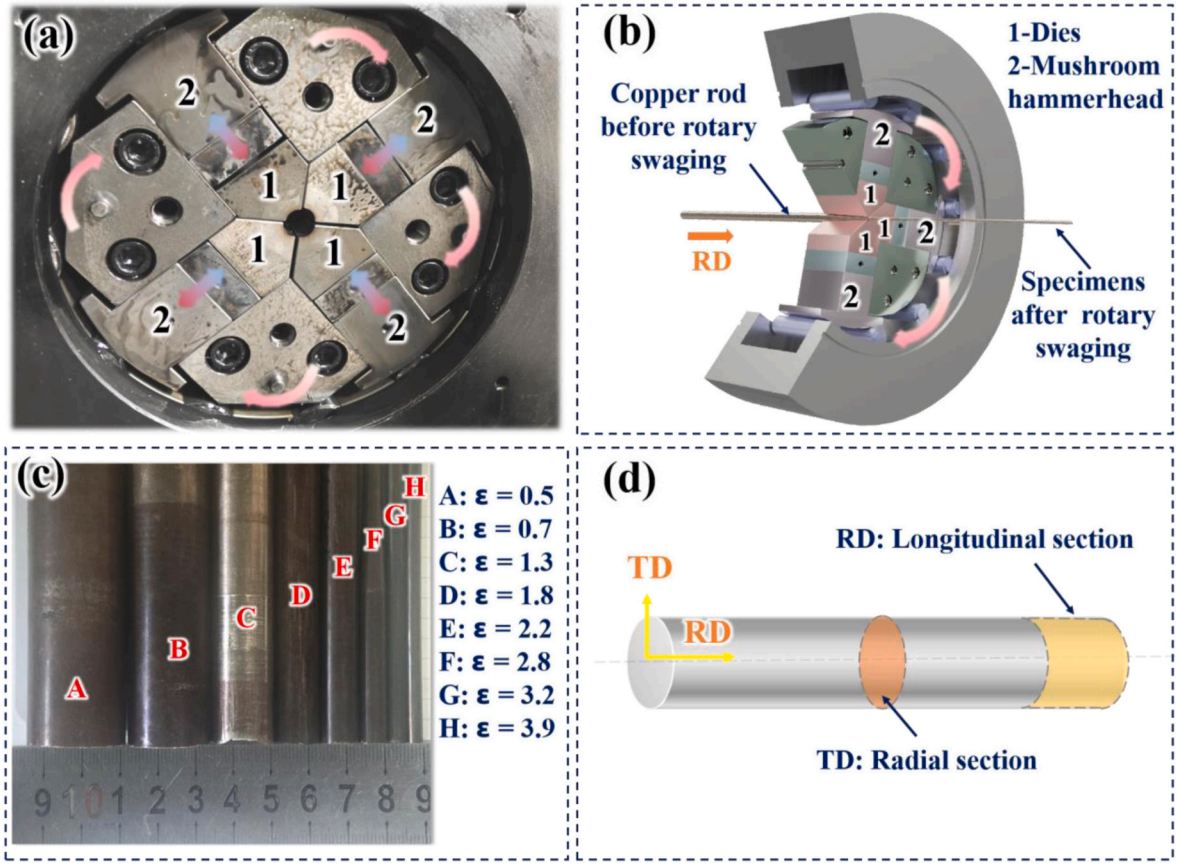

Fig. 2. Rotary swaging process and specimens of the Cu–15Ni–8Sn alloy: (a) Field device diagram; (b) Schematic view of the three-quarter section [5]; (c) Specimens prepared with different rotary swaging deformation; (d) Sampling position of the same rotary swaging samples [6].

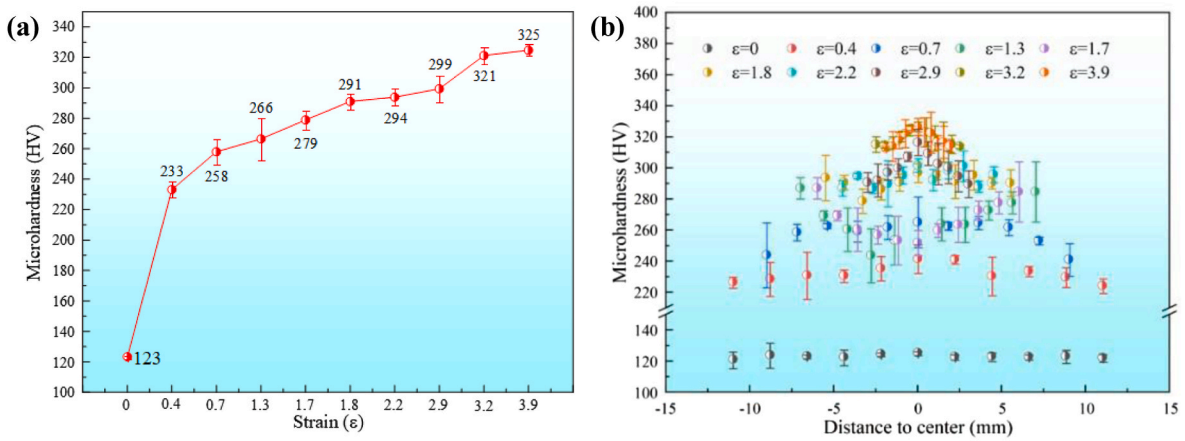

Fig. 3. Microhardness distribution of Cu–15Ni–8Sn alloy after rotary swaging with different strains: (a) Overall distribution image; (b) Distribution image along the diameter direction.

and soft ultrafine grain (UFG) shell, in which the ultimate tensile strength of the NC core reached 1034 MPa [12]. Qingzhong Mao et al. achieved a yield strength of 450 MPa for coarse-grained copper after rotary swaging (equivalent strain ε = 2.5). This deformation caused grain elongation along the swaging axis; the grains reached a length of 340 μm and a diameter of 2 μm, while subgrains attained a length of 25 μm and a diameter of 220 nm [16]. Yuxuan Wang et al. reported that after the rotary swaging treatment (ε = 0.69) of Cu–15Sn–0.3Ti alloy, the tensile strength reached 2.24 times observed in the homogenized annealed state [17]. Lun Zhao et al. demonstrated that after the as-cast Cu–8Sn alloy was subjected to large-strain rotary swaging (ε = 2.9), which effectively relieved the stress concentration and inhibited the micro-crack nucleation [18]. The above studies indicated that compared with drawing and rolling processes, rotary swaging exhibits superior grain refinement and strengthening capabilities in the copper alloys. In addition, our team carried out an exploratory test of rotary swaging cold deformation on high-strength Cu–15Ni–8Sn alloy, and preliminarily verified the feasibility of improving the alloy strength through rotary swaging. For instance, Yanjun Zhou et al. enhanced the tensile strength of the Cu–15Ni–8Sn alloy to 1051 MPa via rotary swaging deformation

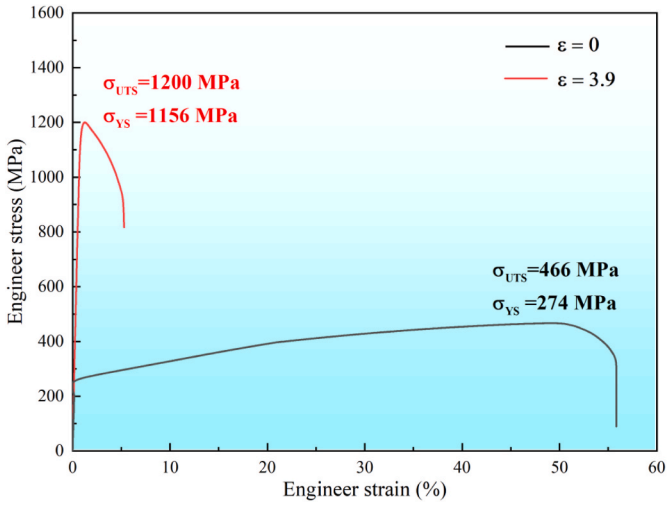

Fig. 4. Engineering stress-strain curves of the Cu–15Ni–8Sn alloy under rotary swaging strain value ε = 0 and ε = 3.9.

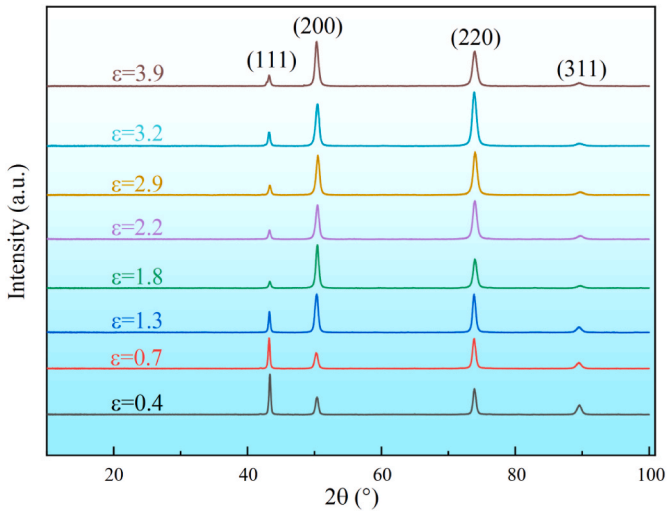

Fig. 5. XRD patterns of the Cu–15Ni–8Sn alloy with different strains after rotary swaging.

(ε = 1.4) [5].

However, for high-strength Cu-15Ni-8Sn alloys, the dynamic microstructure evolution and associated strengthening effects induced by large cumulative strains during continuous rotary swaging have not been systematically and extensively studied. In particular, the following key scientific questions need to be clarified urgently: (1) What are the underlying mechanisms governing the accumulation, evolution, and rearrangement of defects, such as dislocations, deformation twins within the Cu–15Ni–8Sn alloy under continuous large-strain rotary swaging conditions? (2) What is the mechanism of grain refinement that depends only on rotary swaging under large cumulative strain conditions?

Therefore, this paper employs the Cu–15Ni–8Sn alloy to systematically investigate the evolution of mechanical properties under different continuous rotary swaging strains (ε = 0–3.9). Optical microscopy (OM), X-ray diffraction (XRD), electron backscattering diffraction (EBSD), and transmission electron microscopy (TEM) were comprehensively used to analyze the evolution behavior of alloy microstructure (including grain size/morphology, dislocation configuration, twins, texture, etc.) with rotary swaging strain. This paper aims to reveal the grain refinement mechanism of this alloy during continuous rotary swaging, especially the possibility and evolution path of nanocrystalline formation. In addition, the dominant strengthening mechanism of the alloy under the condition of large cumulative strain rotary swaging is proved. The research results can lay a theoretical foundation for breaking through the performance improvement limit of Cu-15Ni-8Sn alloy, and provide technological guidance for its engineering application.

2. Experimental procedures

2.1. Materials and sample preparation

The raw materials are electrolytic copper (≥99.95 wt%), electrolytic nickel (≥99.96 wt%), and pure tin (≥99.99 wt%), which are batched according to the nominal composition. The alloy was smelted by the ZGJT0.025-100-1 vacuum induction furnace to obtain the φ 60 mm × 420 mm ingot. After removing surface defects by mechanical machining, the sample with dimensions φ 40 mm × 375 mm was obtained (the actual chemical composition is shown in Table 1). The specimen was homogenized at 850 °C for 8 h, then air cooled, and then hot rotary swaged to a rod of φ 30 mm × 666 mm. Subsequently, the solution treatment at 850 °C for 1.5 h and water cooling. The average grain size of the solution-treated alloy was 184 μm (Fig. 1 (a)), with no obvious orientation and no unmelted second phase (Fig. 1 (b)). Next, the multi-pass swaging treatment was performed at room temperature. The rotary swaging process of the alloy rod is shown in Table 2. After 16

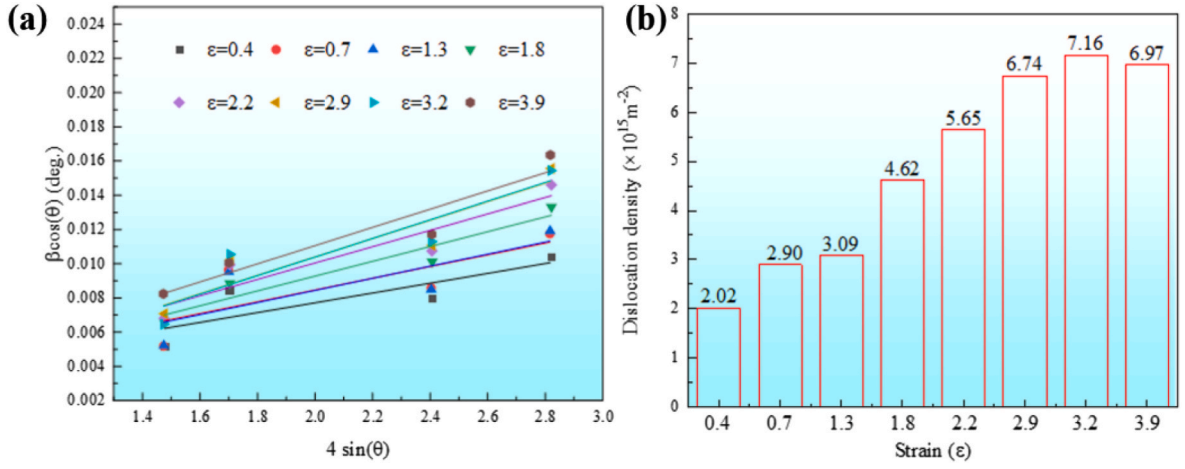

Fig. 6. Calculation of RD plane dislocation density with different strains after rotary swaging of the Cu–15Ni–8Sn alloy: (a) β cost θ - 4 sin θ, (b) Statistical plot of dislocation density.

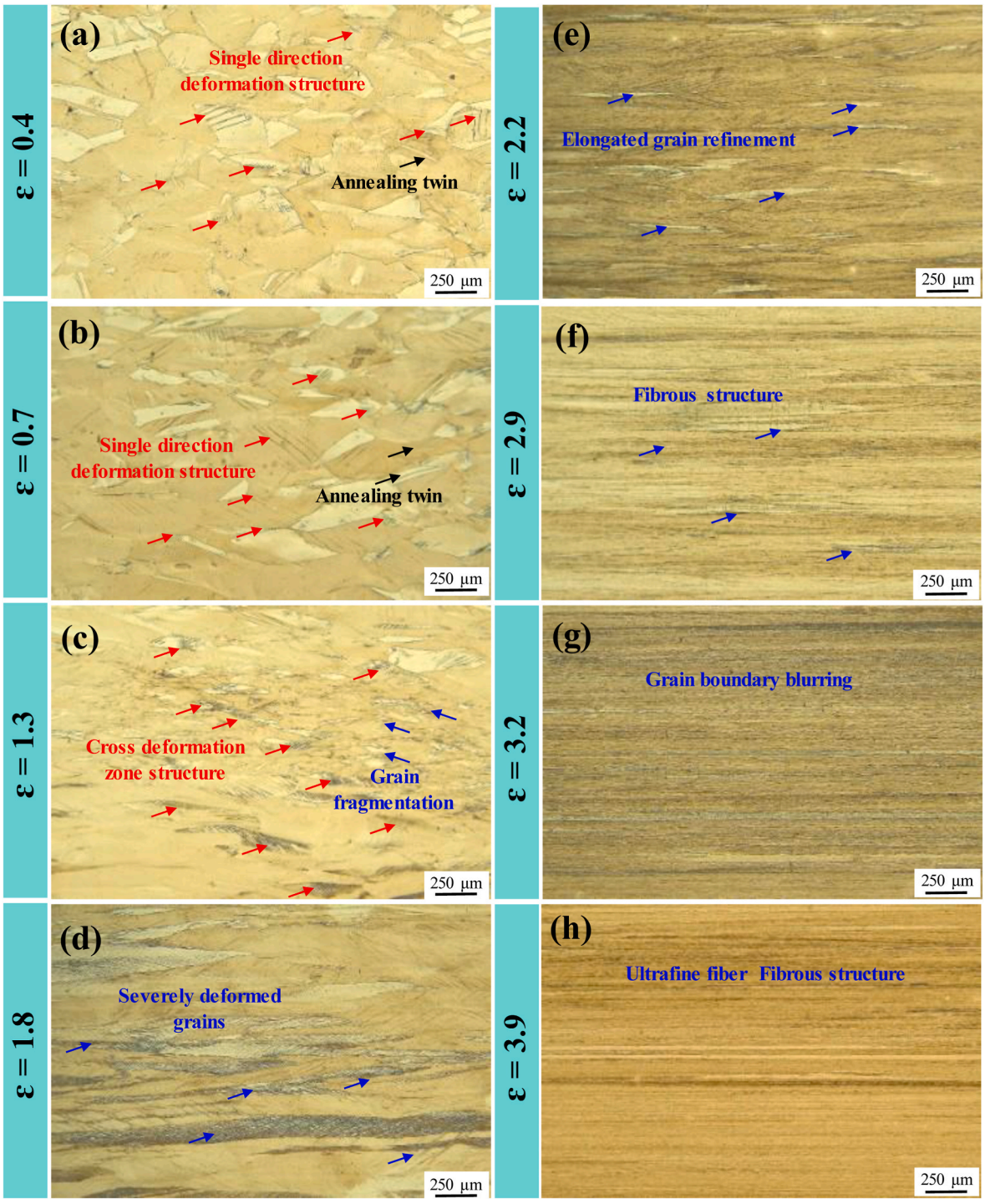

Fig. 7. Metallographic microstructure of the rotary swaged Cu–15Ni–8Sn alloy with different strains (ε = 0.4, 0.7, 1.3, 1.8, 2.2, 2.9, 3.2, 3.9).

consecutive processes, the diameter of the alloy rod reaches φ 4.2 mm, and the equivalent strain ε is 3.9. The schematic diagram of the rotary swaging process is shown in Fig. 2. The equivalent strain ε is calculated as: $\varepsilon = \ln\left(\frac{A_0}{A}\right)$, where A_0 is the original cross-sectional area and A is the final cross-sectional area [20]. Additionally, in this paper, the longitudinal section direction is defined as the rotary swaging direction (RD).

2.2. Microstructure characterization

The samples were cut along the longitudinal section (RD) by electric spark cutting, mechanically sanded and polished using diamond sandpaper (400, 800, 1200, 2000, 5000), diamond suspensions at 1 μm and 0.25 μm. Corrosion was carried out with aqueous solution of ferric chloride hydrochloric acid (5 g $FeCl_3$ + 10 ml HCl + 100 ml water). The metallographic structure of the samples was observed by the Leica DM6M upright optical microscope. Subsequently, the mechanically polished and polished samples were subjected to vibration polishing using the VP-430 vibration polisher (polishing solution: 50 nm SiO_2) for 6 h. The microstructure of the sample is Zeiss Gemini 360, and the EBSD model is Oxford Symmetry S3. The SEM acceleration voltage used during the test is 20 kV, the beam current is 13 nA, and the step sizes are 1.8

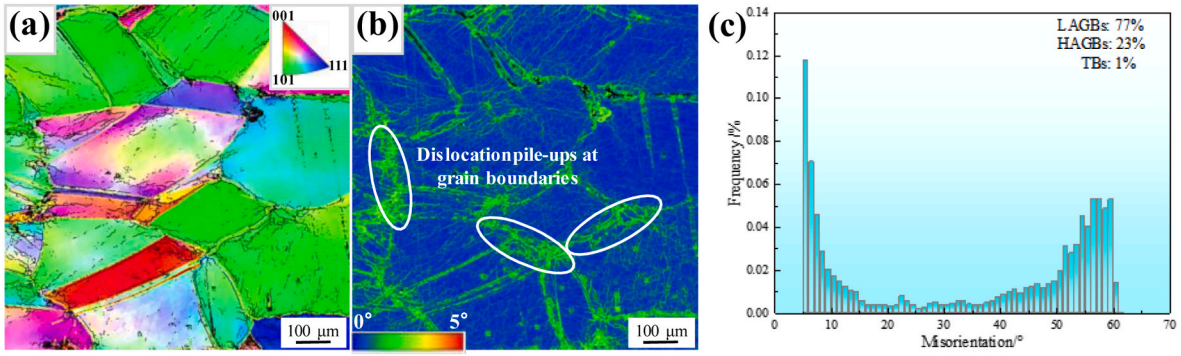

Fig. 8. EBSD analysis of the rotary swaged Cu–15Ni–8Sn with strain ε = 0.4: (a) IPF; (b) KAM; (c) Statistical plot of GBs.

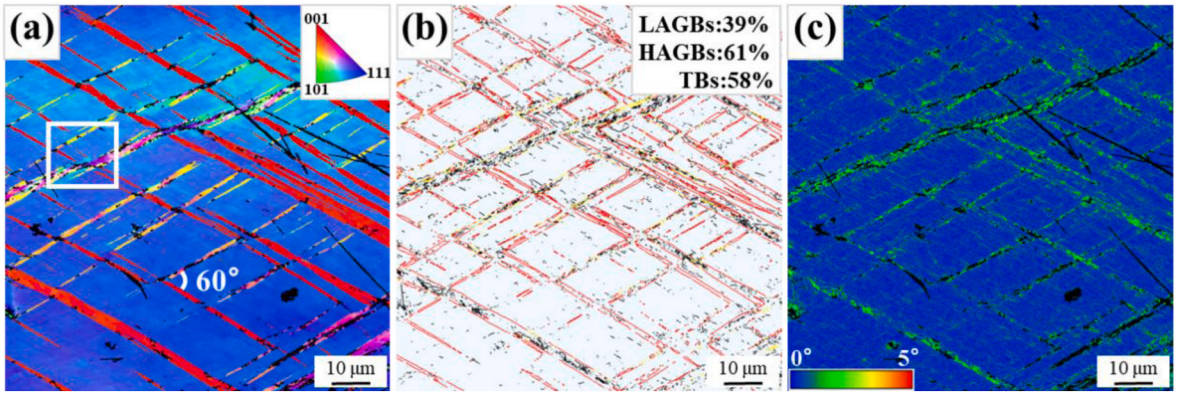

Fig. 9. EBSD analysis of the rotary swaged Cu–15Ni–8Sn alloy with strain ε = 1.3: (a) IPF; (b) GBs; (c) KAM.

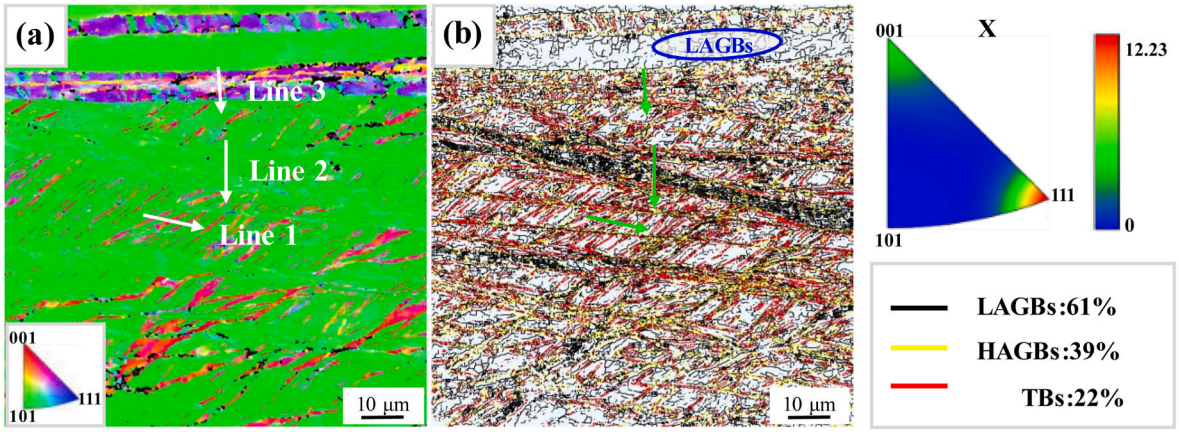

Fig. 10. EBSD analysis of the rotary swaged Cu–15Ni–8Sn alloy with strain ε = 1.8: (a) IPF; (b) GBs.

μm (Fig. 8), 0.18 μm (Figs. 9 and 10), and 0.007 μm (Figs. 11 and 12), respectively. The XRD data were obtained by Empyrean X-ray diffractometer, the tube voltage was 40 KV, the tube current was 30 mA, the scanning speed was 6°/min, and the scanning angle 2θ range was 10–100°. The test data were analyzed by MDI Jade5.0 software. Using FEI Talos F200X transmission electron microscope, the longitudinal section of the sample without strain was analyzed by TEM, and the acceleration voltage was 200 kV. The bright field images, dark field images, selected area electron diffraction patterns and high-resolution images were obtained respectively. The test samples were prepared using the electrolytic polishing and electrolytic etching equipment (etching solution: 5 % perchloric acid + 95 % ethanol, reaction temperature: −30 °C, reaction parameters: 40 V). It should be noted that in this paper, the sampling locations for the microstructural analysis of the longitudinal sections (RD) of the alloy specimens were all from the core regions, and the horizontal directions of the images captured were parallel to the rotary swaging direction (RD).

2.3. Mechanical properties test

For the longitudinal section (RD) specimen after wire electrical discharge machining, the specimen was firstly inlaid with an inlay solution composed of acrylic powder and curing agent in a ratio of 5:4. Next, the sample was gradually polished from P1000 silicon carbide waterproof sandpaper to P2000. Subsequently, the specimens were finely polished using the 0.25 μm diamond suspension. Finally, the

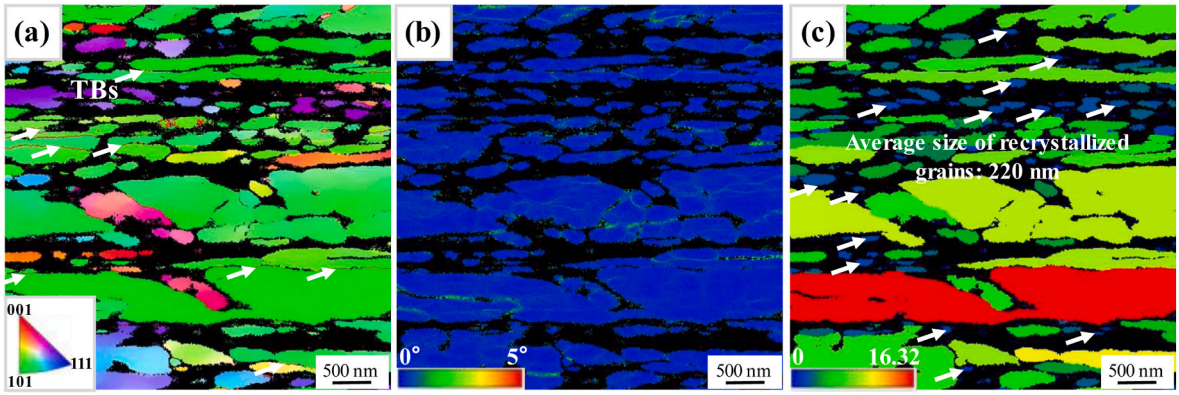

Fig. 11. EBSD analysis of the rotary swaged Cu–15Ni–8Sn alloy with strain ε = 2.9: (a) IPF + GBs; (b) KAM; (c) GOS.

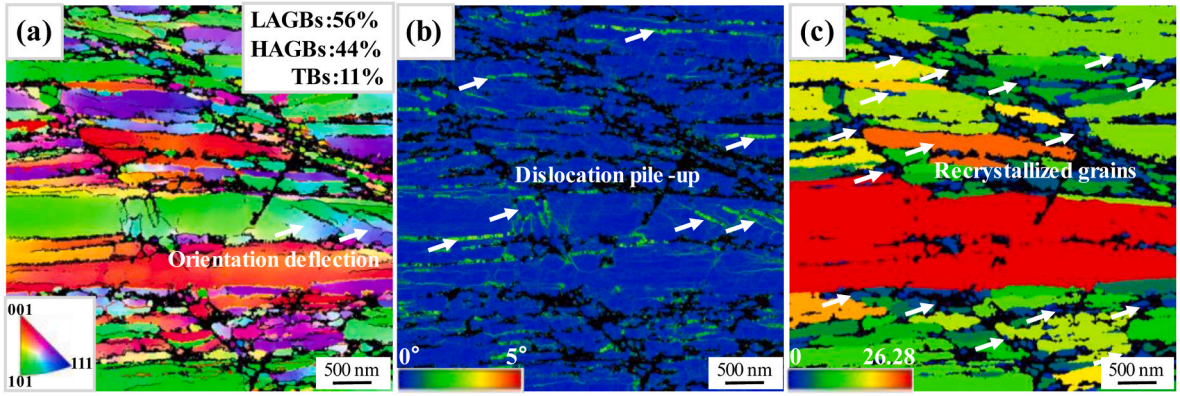

Fig. 12. EBSD analysis of the rotary swaged Cu–15Ni–8Sn alloy with strain ε = 3.9: (a) IPF + GBs; (b) KAM; (c) GOS.

microhardness of the sample was measured by QHV−1000TPTA automatic Vickers hardness tester under the conditions of loading force of 200 g and holding time of 10 s. The microhardness measurement was performed on the RD plane along the diameter (TD) direction, and three test routes were set up. Place 11 points on each test route, of which the sixth point is the center position of the line, and the starting point of the three test routes and the sample boundary, between two adjacent points, and the distance between any two routes along the diameter are consistent. The overall hardness of the specimen is based on the average hardness obtained after eliminating the maximum and minimum values of the three test routes, respectively. Rod-shaped tensile samples were prepared in accordance with the national standard GB/228. 1−2021 "Tensile Testing of Metal Materials Part 1: Room Temperature Test Method". The total length of the rod-shaped tensile specimen was 40 mm. Among them, the diameter and gauge length of the middle section are 3 mm and 15 mm, respectively.The tensile strength of the alloy was tested using the UTM4304 tensile testing machine. The tensile rate was 1 mm/min, and the average value of 3 parallel samples was taken as the test result.

3. Results

3.1. Mechanical property

Fig. 3 shows the microhardness distribution of the Cu–15Ni–8Sn alloy after rotary swaging at different strain. It can be seen from Fig. 3 (a) that before deformation, the hardness of the solution-treated Cu–15Ni–8Sn alloy is 123 HV. With the gradual increase of strain, the overall hardness of the alloy shows a monotonic increasing trend. When the strain value ε = 0.4, the overall hardness value of alloy reaches 233 HV, which is 89 % higher than that of the solid solution state. When the strain reaches 3.2, the overall hardness value of alloy is 321 HV. Continuing to increase the strain to 3.9, the overall hardness value of the alloy shows slow growth trend, reaching 325 HV, which is 164 % higher than that of the solid solution state. Fig. 3 (b) reveals the distribution of microhardness along the diameter direction of Cu–15Ni–8Sn alloy after rotary swaging. It can be found that the microhardness distribution along the diameter direction is obviously different under different strains. For the Cu–15Ni–8Sn alloy in solid solution, the core and edge hardness values of the specimen are equivalent and distributed uniformly.

Furthermore, we selected the specimens with strain ε = 0 and ε = 3.9 for tensile test respectively. Fig. 4 shows the engineering stress-strain curves of the Cu–15Ni–8Sn alloy with rotary swaging strains value ε = 0 and ε = 3.9. It can be seen that when the strain value ε = 3.9, the tensile strength, yield strength, and elongation of the alloy reach 1200 MPa, 1156 MPa, and 4.76 %, respectively. The tensile strength and yield strength are increased by 1.58 times and 3.22 times, respectively, compared with the undeformed state (ε = 0).

3.2. Macro-texture and dislocation density

Fig. 5 presents the XRD patterns of the Cu–15Ni–8Sn alloy after rotary swaging with different strains. With the increase of rotary swaging strain, the intensity of (111) peak in XRD pattern of alloy decreases gradually, while the intensity of (220) peak and (200) peak gradually increases. It shows that the obvious preferred orientation of grains occurs after rotary swaging deformation.

The strength improvement of the alloy caused by rotary swaging deformation must be related to the dislocation density. The dislocation density ρ of the rotary swaged Cu–15Ni–8Sn alloy sample can be approximately calculated by the following formula [8,19]:

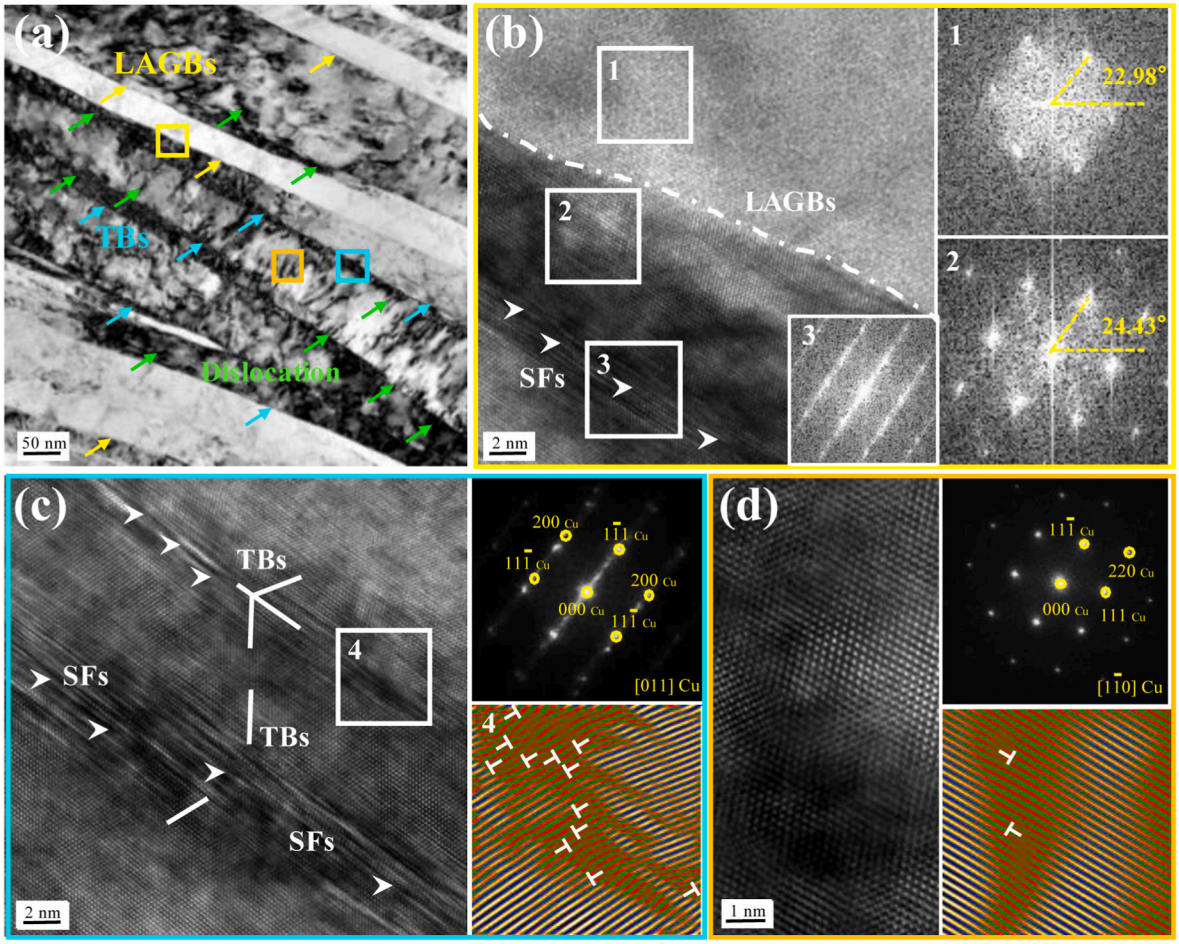

Fig. 13. TEM images of the rotary swaged Cu–15Ni–8Sn alloy with strain ε = 2.2: (a) Bright field image; (b) HRTEM of the deformation band interface; (c) HRTEM of twin boundaries; (d) HRTEM of matrix.

$$\rho = 16.1(\varepsilon/b)^2 \quad (1)$$

Where, ε is the micro-strain, which is calculated from XRD pattern, and the equation is:

$$\beta\cos(\theta) = (K\lambda)/d + 4\varepsilon\sin(\theta) \quad (2)$$

Where β is the width at half maximum (FWFM) at the maximum of the XRD diffraction peak; λ is the radiation wavelength (λ = 0.154 nm); K is a constant (K ≈ 0.9); θ is the Bragg angle and d is the average grain size.

Fig. 6 (a) illustrates the linear relationship of "β cost θ - 4 sin θ" to obtain the microscopic strain ε diagram, while Fig. 6 (b) shows the dislocation density distribution diagram obtained by substituting the microstrain into equation (1). It can be observed that with the increase of rotary swaging strain, the dislocation density shows a continuous increasing trend. When the strain reaches 3.2, the dislocation density reaches the maximum value. Continues to increase the strain to 3.9, and the dislocation density decreases slightly, which is 6.97 × 10^{15} m^{-2}.

3.3. Evolution of microstructure

Fig. 7 reveals the metallographic microstructure of the Cu–15Ni–8Sn alloy under different rotary swaging strains. At strain of ε = 0.4, the grain is coarse while it was slightly elongated along axis direction. Some extremely thick twins which should be caused by Solid solution heat treatment could be observed. At a strain value of 1.3, the deformed grains of the alloy are elongated, and the staggered deformation structure appears in the smaller grains, and some grains are fragmented. When the strain reaches 1.8, the deformed grains of the alloy are further elongated, and more grains participate in the coordinated deformation, and severely deformed grains are evident. As the strain value increases to 2.2, the deformed microstructure becomes finer. With further increases in strain value from 2.9 to 3.9, the grain boundaries and deformed structures became blurred, resulting in a dense ultrafine fibrous microstructure.

3.3.1. EBSD analysis

Fig. 8 displays the IPF (Inverse Pole Figure) and KAM (Kernel Average Misorientation) of the rotary swaged Cu–15Ni–8Sn alloy with strain ε = 0.4. As observed, the grains did not experience significant tensile deformation during the initial stage of rotary swaging. Mainly composed of annealed twins, accounting for only 1 %, and no deformed twins were detected. Additionally, combined with the distribution of grain boundary positions in Fig. 8(a) and (b), it can be found that numerous Geometrically Necessary Dislocations (GNDs) are generated within the grains to accommodate intragranular deformation [23]. We define the orientation difference of adjacent grains greater than 15° as high-angle grain boundaries (HAGBs) and less than 15° as low-angle grain boundaries (LAGBs). The proportion of the low-angle grain boundaries in Fig. 8 (c) is 77 %.

Fig. 9 is the EBSD analysis of the rotary swaged Cu–15Ni–8Sn alloy with strain ε = 1.3. It can be seen that when the strain increases to 1.3, plenty of deformation twins [21] appear on the close packed plane (111) (Fig. 9 (b), the proportion of twins is 52 %), and the twins cross each other at an included angle of 60°. The twins contain a high density of dislocations. According to the KAM diagram of Fig. 9 (c), the

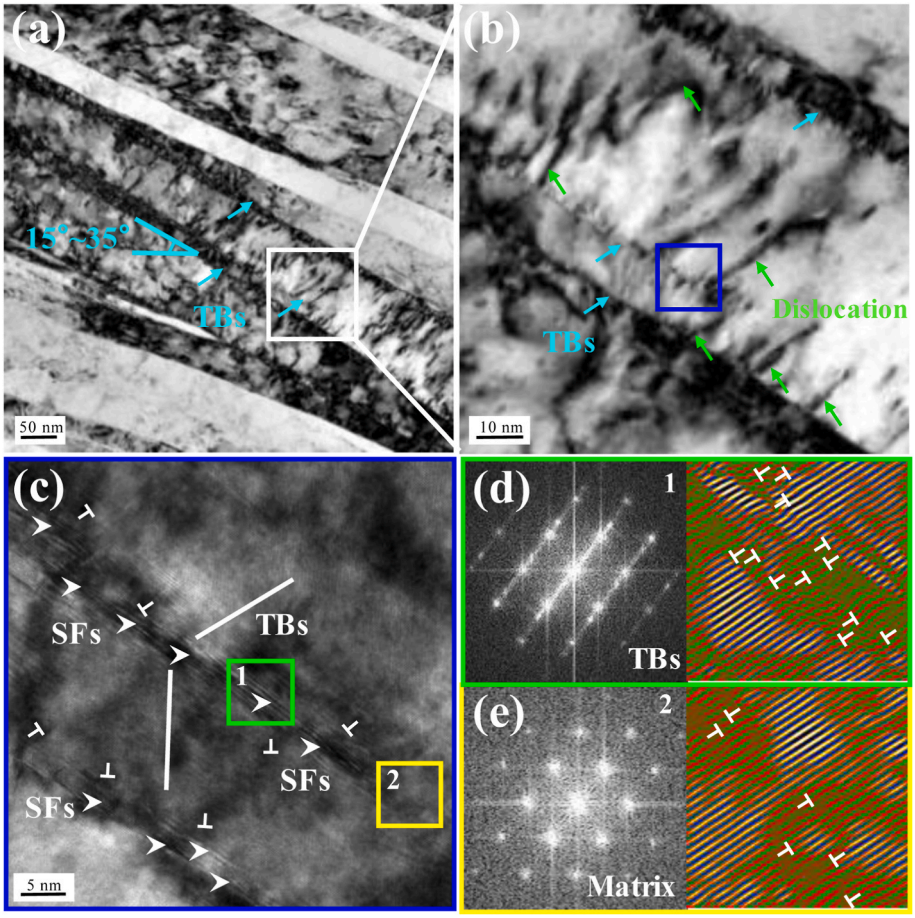

Fig. 14. TEM images of the rotary swaged Cu–15Ni–8Sn alloy with strain ε = 2.2: (a) Bright field image; (b) Enlarged view of the white boxed area in Fig. (a); (c) High-resolution images of nanotwin ends; (d) SADE and dislocation distribution diagram of nanotwin; (e) Electron diffraction and dislocation distribution diagram of matrix selection at the end of nanotwins.

accumulation of dislocations within the twins is due to the restricted movement of dislocations within the twin interiors.

Fig. 10 is the EBSD analysis of the rotary swaged Cu–15Ni–8Sn alloy with strain ε = 1.8. It can be clearly seen from Fig. 10 (a) that the alloy has obvious texture. When the strain ε = 1.8, the alloy presents double texture, in which <111 > orientation is strong and <100 > orientation is relatively weak. Compared with strain ε = 1.3, the microstructure of alloy with strain ε = 1.8 is obviously refined, and the denser deformation structure appears, and a mass of small LABGs and twins are distributed in the deformation zone. The proportion of small angle grain boundaries increased from 39 % to 61 %.

Fig. 11 is the EBSD analysis of the rotary swaged Cu–15Ni–8Sn alloy with strain ε = 2.9. When the strain increases to 2.9, the twin characteristics are obviously different from the staggered distribution at ε = 1.8, but parallel to the RD direction of rotary swaging. Fig. 11 (c) is a GOS diagram, and the GOS (Grain Orientation Spread) diagram can be used to distinguish recrystallized grains. The recrystallized grains generally have lower GOS values because they undergo lattice rearrangements during recrystallization, have less internal strain and are more uniformly oriented [25]. In Fig. 11, blue indicates recrystallized grains, red indicates deformed grains, and yellow indicates substructure. It can be seen that when the rotary swaging strain is 2.9, recrystallization occurs inside the alloy, and the average size of recrystallized grains is 220 nm according to statistics.

Fig. 12 is the EBSD analysis of the rotary swaged Cu–15Ni–8Sn alloy with strain ε = 3.9. The layered structure was further refined and ultrafine grains were formed. According to statistics, the average grain size is 1.23 μm. A multitude of rainbow color distributions appear inside the layered structure, indicating that the dislocation motion causes lattice rotation [26]. The dislocation wall formed by dislocation pile-up forms a small angle grain boundary in the process of continuous pile-up, and the small angle grain boundary accounts for 56 %. It can be seen from Fig. 12 (b) that the dislocation wall formed by intragranular pile-up further segments the layered grains. The continuously increasing stress concentration further promotes the occurrence of recrystallization. According to the GOS diagram shown in Fig. 12 (c), it can be found that the recrystallized grains are obviously smaller and distributed more.

3.3.2. *TEM analysis*

Fig. 13 presents the TEM images of the rotary swaged Cu–15Ni–8Sn alloy with strain ε = 2.2. As observed, the alloy microstructure is mainly composed of lamellar subgrains, which contain a high density of dislocations and deformation twins. Both the lamellar subgrains and the twin boundaries act as barriers to dislocation motion, resulting in dislocation pile-ups. Moreover, the twin boundaries are all straight interfaces. Fig. 13 (b) shows the low-angle grain boundaries (LAGBs) formed by dislocation pile-up, while there is a quantity of stacking faults. And the stress will lead to the further evolution of stacking faults into twins [27]. As shown in Fig. 13 (c), there are still many stacking faults and dislocations distributed in the twin. Fig. 13 (d) depicts the copper matrix, which can be determined as a fcc structure by selecting electron diffraction calibration, and no phase transformation structure is found. In addition, it can also be found from Fig. 14 that the fine twins are hindered by dislocations at the growth front and terminate. The crystallographic orientation relationship between the twins and the matrix is determined. The spatial distribution characteristics of twins and matrix

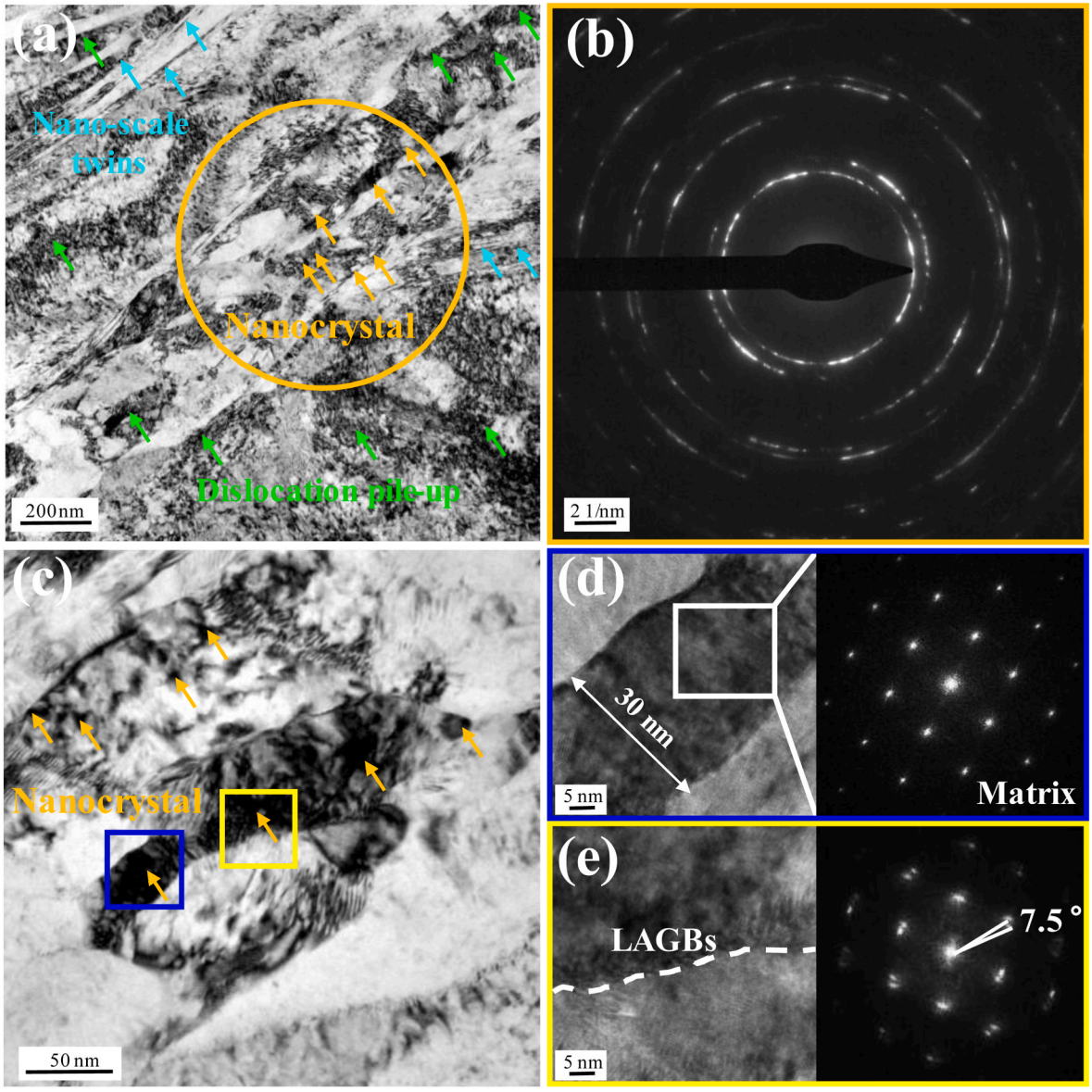

Fig. 15. TEM images of the rotary swaged Cu–15Ni–8Sn alloy with strain ε = 3.2: (a) Bright field image; (b) Nanocrystalline selective electron diffraction; (c) Nanocrystalline bright field image; (d) HRTEM and SADE of nanocrystals in blue frame region in Fig. (c); (e) High-resolution image of nanocrystal boundary in yellow box region and SADE in Fig. (c). (For interpretation of the references to color in this figure legend, the reader is referred to the Web version of this article.)

during rotary swaging, showing 15–35° from RD direction (Fig. 14).

Fig. 15 is the TEM image of the rotary swaged Cu–15Ni–8Sn alloy with strain ε = 3.2. It can be seen that when the strain reaches 3.2, the core region of the alloy exhibits a high density of dislocations, which are intertwined and pile up to form deformation bands [28]. Large deformation also induces numerous nanotwins, and the twin interface is relatively straight (Fig. 15 (a)). It is worth noting that the SADE in the orange region in Fig. 15 (a) (as shown in Fig. 15 (b)) presents concentric rings, which indicates that nanocrystals appear in the internal structure of the alloy [29]. A detailed analysis of the nanocrystals is shown in Fig. 15(c). The nanocrystalline size is below 100 nm, and the angle of grain boundaries between nanocrystals is 7.5° (Fig. 15 (d)), which is a low-angle grain boundaries (LAGBs).

Fig. 16 shows the TEM images of the rotary swaged Cu–15Ni–8Sn alloy with strain ε = 3.9. As observed in the images, the deformed microstructure is significantly refined, and the direction is basically parallel to the RD direction. Fig. 16 (d) indicates that the width of lamellar grains are bounded by high-angle grain boundaries (HAGBs). The measured size of the lamellar grains in Fig. 16(a) is 45 nm. Secondary nanotwins are formed within the lamellar grains (Fig. 16(b)), with a twin layer thickness ranging from 1 to 10 nm. Fig. 16(c) is a dark-field image, revealing a high density of dislocations. High-resolution observation of nanotwins is performed, as shown in Fig. 16 (d). Nanotwins interact with a high density of dislocations, and numerous stacking faults are distributed. Therefore, it is revealed that after rotary swaging at large-strain (ε = 3.9), the whole matrix of the alloy predominantly exhibits a multiscale microstructure characterized by high-density dislocations and layered fine grains, while locally, nanotwins, and nanocrystals are also established.

However, according to the TEM images of the RD surface of the alloy shown in Fig. 16, it can be speculated that the nanometer-sized layered grains and twins of the RD plane may all be nanocrystalline on the TD plane. Therefore, TEM analysis of TD surface core of Cu–15Ni–8Sn alloy with rotary swaging strain ε = 3.9 is carried out. The results are shown in Fig. 17, polycrystalline rings appear, indicating the formation of numerous nanocrystals in the alloy.

In order to make a more detailed exploration of the nanocrystals in the core of TD plane of the rotary swaged Cu–15Ni–8Sn alloy

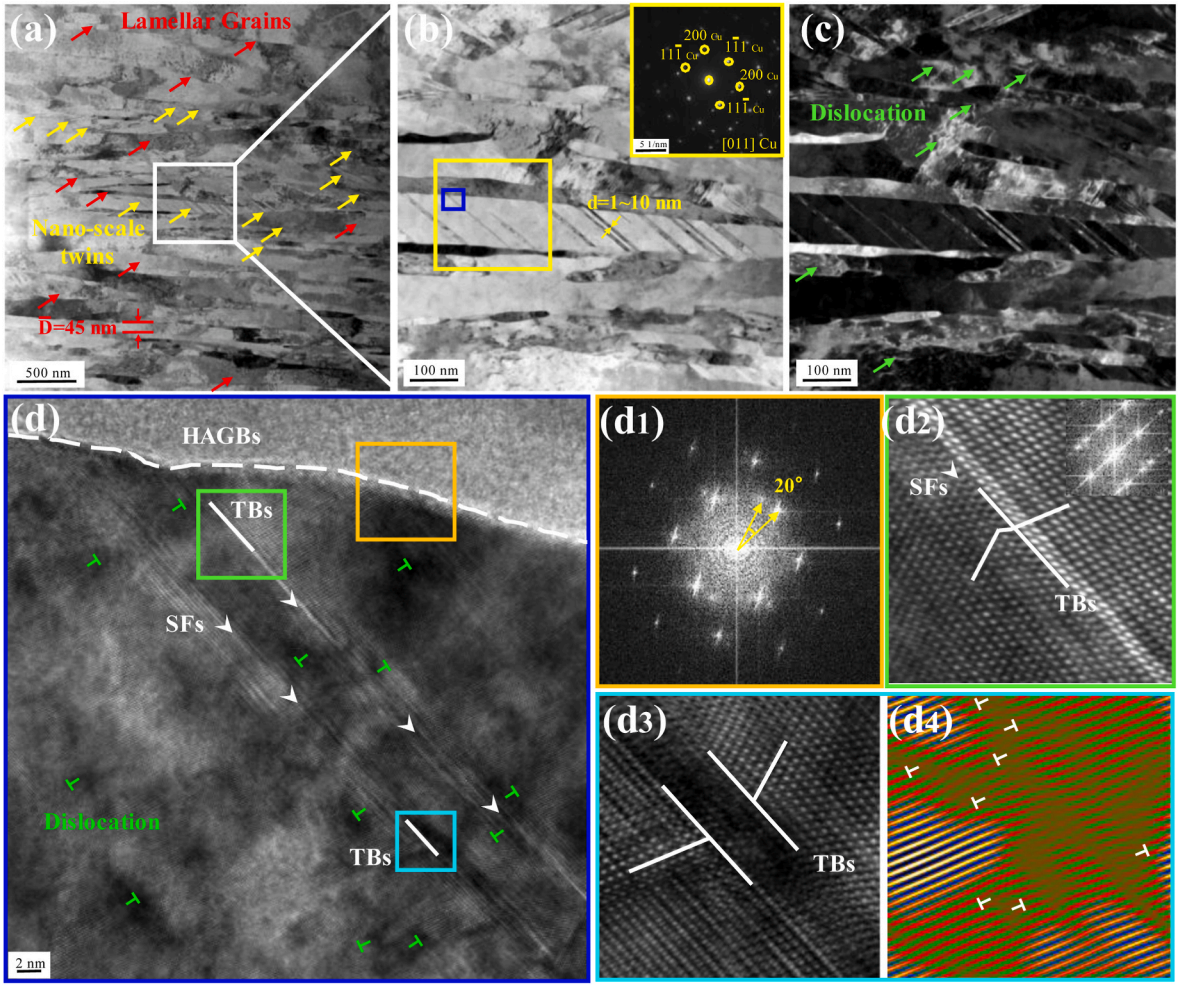

Fig. 16. TEM images of the rotary swaged Cu–15Ni–8Sn alloy with strain ε = 3.9: (a) Bright field image; (b) Fig. (a) Bright field image of nanotwin region; (c) Dark field image corresponding to fig. (b); (d) High-resolution image of the blue boxed area in Fig. (b). (For interpretation of the references to color in this figure legend, the reader is referred to the Web version of this article.)

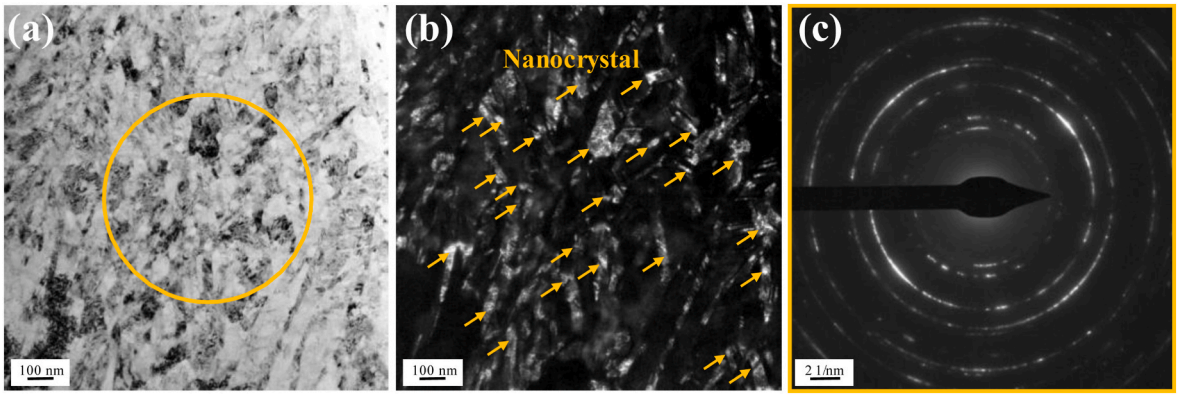

Fig. 17. TEM images of TD surface core of rotary swaged Cu–15Ni–8Sn alloy with strain ε = 3.9: (a) Bright field image; (b) Dark field image; (c) the orange region in Fig. (a) corresponds to the selected area electron diffraction. (For interpretation of the references to color in this figure legend, the reader is referred to the Web version of this article.)

corresponding to the strain 3.9, the nanocrystalline region in the alloy is analyzed with HRTEM and SADE, as shown in Fig. 18. And we can see an abundance of nanocrystals, including spherical, rhombic, rectangular, irregular patterns, etc (Fig. 18 (a)). The average grain size of nanocrystals is 18 nm statistically calculated by Image J software. Fig. 18 (b) is a dark field image, and it can be seen that there are a quantity of dislocations and a small number of twins inside the grain. The high-resolution image of nanocrystalline transmission electron microscope is shown in Fig. 18 (c). The white dashed line in the figure outlines the nanocrystalline interface. We perform Fourier changes on the position around region 1 to obtain the FFT image. It can be seen that the angle between regions 2, 3, 4, 5 and region 1 is between 2 and 7°, which is a

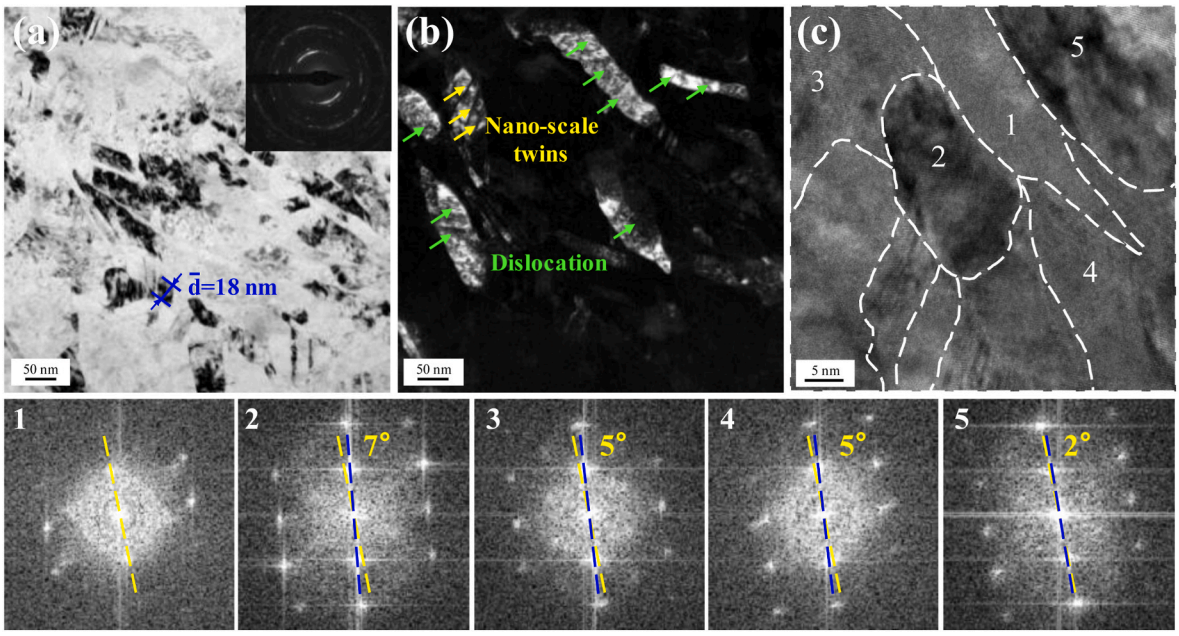

Fig. 18. TEM images of TD surface core of rotary swaged Cu–15Ni–8Sn alloy with strain 3.9: (a) Bright field image; (b) Dark field image; (c) High-resolution images of nanocrystals.

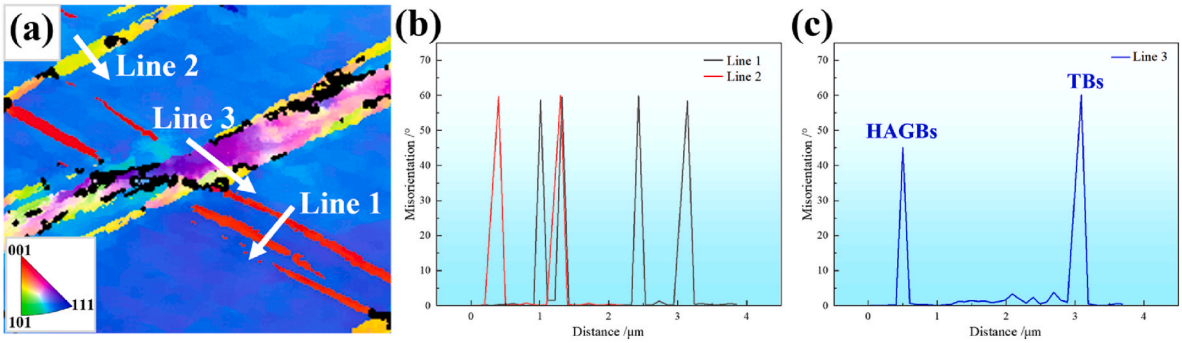

Fig. 19. EBSD analysis of the rotary swaged Cu–15Ni–8Sn alloy with strain ε = 1.3: (a) Partial view of white frame line in Fig. 11 (a); (b–c) Point-to-point orientation distribution plot of the three white lines in Fig. (a).

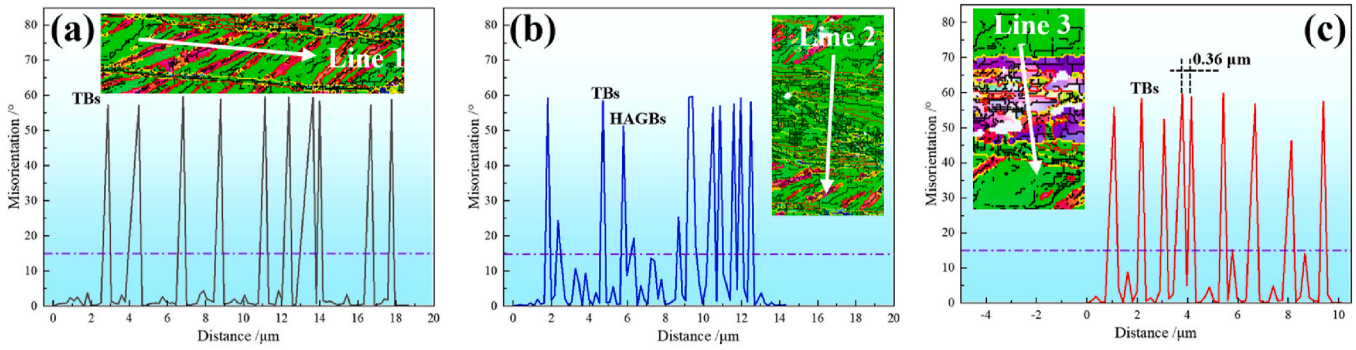

Fig. 20. EBSD analysis of the rotary swaged Cu–15Ni–8Sn alloy with strain ε = 1.8: (a–c) Point-to-point orientation distribution diagram of lines 1, 2, and 3 in Fig. 11 (a).

small-angle grain boundary.

4. Discussion

4.1. Mechanism of microstructure evolution

The evolution law of typical microstructure characteristic nodes of Cu–15Ni–8Sn alloy under large strain rotary swaging can be

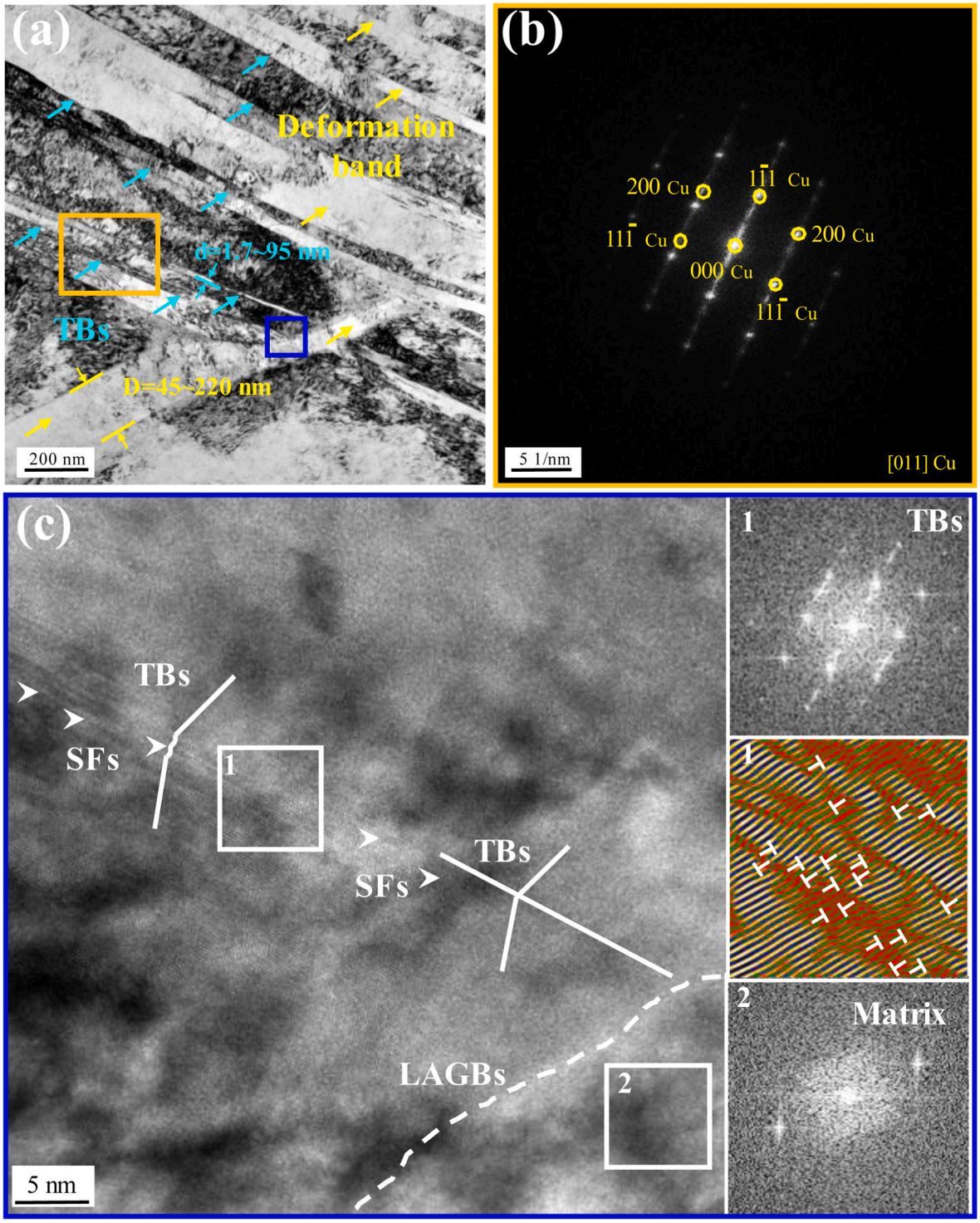

Fig. 21. TEM images of the rotary swaged Cu–15Ni–8Sn alloy with strain ε = 2.2: (a) Bright field image; (b) Nanotwin selective electron diffraction; (c) High-resolution image and Fourier transform diagram of the interaction position of nanotwins and LAGBs.

summarized as follows: Dislocation → Cross twins (ε ≥ 1.3) → Layered fine grains (ε ≥ 1.8) → Nanotwins (ε ≥ 2.2) → Nanocrystals (ε ≥ 3.2).

Stage 1: Dislocation-dominated deformation mechanism. At the initial stage of rotary swaging of Cu–15Ni–8Sn alloy (ε ≤ 0.4), a great deal of geometrically necessary dislocations occur in the coarse grains, thus forming high-density dislocation walls [26]. In Fig. 10 (a), the color gradient appears inside a single grain, showing a rainbow color, which represents that the grain tilts during the deformation process. This tilt helps to coordinate the deformation.

Stage 2: Cross-twin coordinated deformation mechanism. When the rotary swaging strain ε = 1.3, combined with Figs. 9 (a) and Fig. 19, it is found that with the further increase of rotary swaging strain, twins become the main mechanism to coordinate the deformation of Cu-15Ni-8Sn alloy on the basis of dislocation motion. The cross twinning can effectively disperse the stress and improve the deformation ability of the alloy [4,24,30].

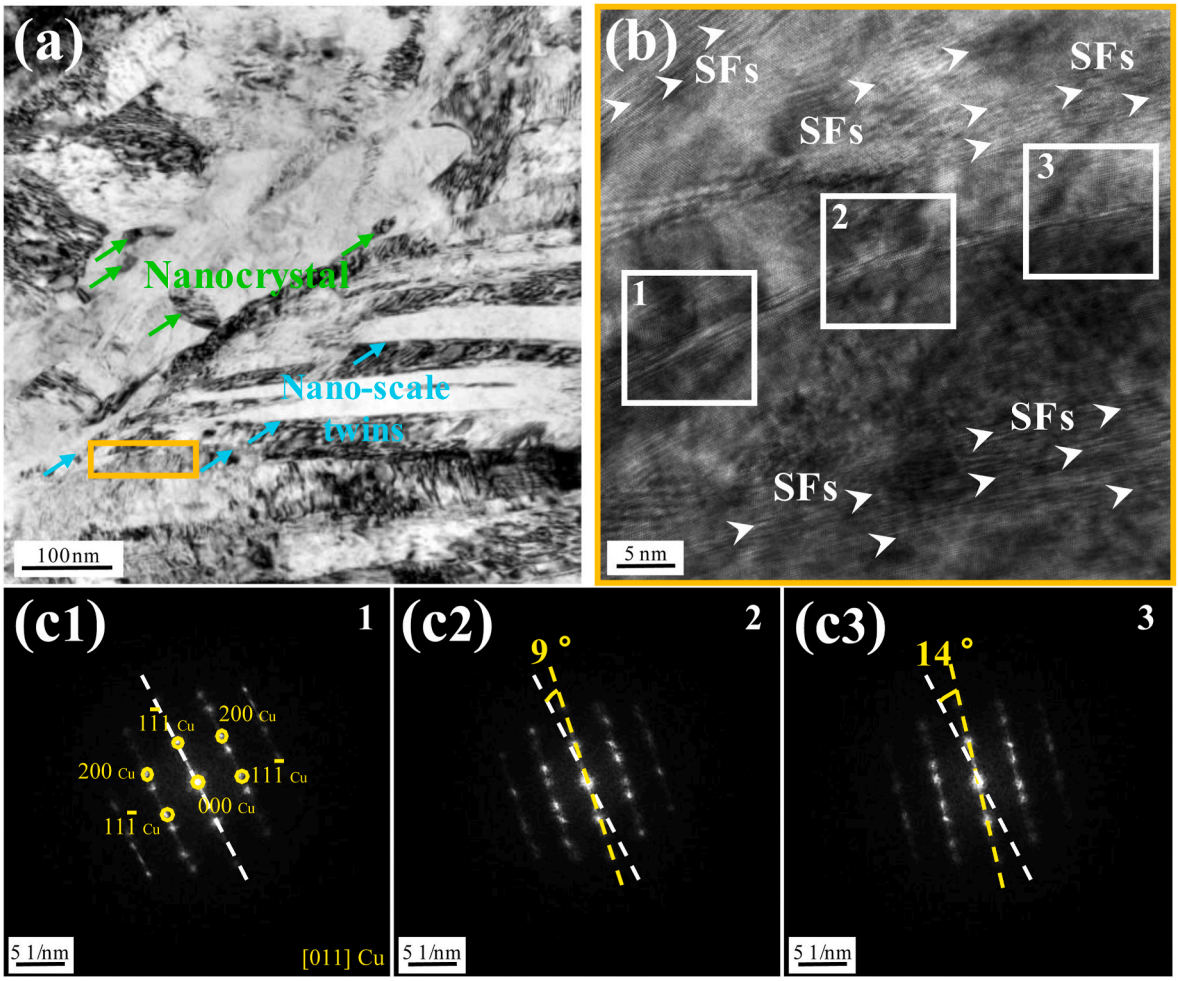

Fig. 22. TEM diagram of the rotary swaged Cu–15Ni–8Sn alloy with strain ε = 3.2: (a) Bright field image; (b) High-resolution images of tilt twin boundaries; (c1-3) Select electron diffraction in regions 1, 2, and 3 in Fig. (b).

Stage 3: Formation of layered fine grain. By analyzing Figs. 10 (a) and Fig. 20, we find that fine cross-deformation twins appear in the Cu-15Ni-8Sn alloy with the increase of the rotary swaging strain. This result makes the deformed microstructure of the alloy further refined, forming layered fine grains [31].

Stage 4: Further coordinated deformation of nanotwins. When the rotary swaging strain ε = 2.2, as depicted in Fig. 21, nanotwins indeed emerge within the core grains of RD plane of Cu–15Ni–8Sn alloy. These nanotwins exhibit spacings ranging from 1.7 to 95 nm, with their growth fronts arrested by low-angle grain boundaries (LAGBs) formed through dislocation pile-ups. The synergistic effect of LAGBs and nanotwins can also achieve multiple refinements of microstructures at submicron and even nanometer scales [32,33].

Stage 5: Local formation of nanocrystals and continuous refinement of layered structures. Previous studies have shown that high temperature will inevitably be generated in the rotary swaging process, and shows that local heating of several hundred degrees Celsius will be generated in the high-frequency loading process, and the heat will be dissipated in a very short time [34–36]. The instantaneous high temperature and high strain rate may trigger the dynamic recrystallization mechanism [37,38]. When the strain is 2.9, the continuously increasing strain energy provides a driving force for recrystallization, resulting in local nanocrystals in Cu–15Ni–8Sn alloy, as shown in Fig. 11. The formation of recrystallized grains makes the microstructure inside the alloy more uniform, thereby improving the coordinated deformation ability of the alloy.

When the rotary swaging strain reaches 3.2, the dislocation density continues to increase, and the interaction between dislocations and deformation zones, twin boundaries and stacking faults continues to increase. However, when the accumulated deformation of rotary swaging is large enough, we find that unlike the nanotwins with the flat and straight interface in Fig. 15 (a), the twin boundary has tilted, as shown in Fig. 22. A detailed analysis of the HRTEM of the tilted nanotwin interface (Fig. 22 (c)) shows that the lattice on both sides of the twin boundary is deflected at equal angles. As we have observed in Fig. 23, when the rotary swaging strain reaches 3.9, the layered structure is further refined. The layered grain boundaries have not only high-angle grain boundaries (HAGBs) but also low-angle grain boundaries (LAGBs) (as shown in Fig. 23(e and f)). The dislocations inside the nanotwins will rearrange to form dislocation wall with the bamboo-like morphology (as shown in Fig. 23 (d)), thus dividing the twins into nano-sized slender blocks, which also provides conditions for the formation of nanocrystals (see Fig. 24).

4.2. Analysis of strengthening mechanism

As demonstrated in Fig. 4, the yield strength of Cu–15Ni–8Sn alloy is 1156 MPa when the rotary swaging strain ε = 3.9, which is 3.22 times higher than that of the solid solution alloy of 274 MPa. The observed strengthening primarily arises from the synergistic contributions of high dislocation density, grain refinement, and solution strengthening. And then the contribution of various strengthening methods to the yield strength of rotary swaged Cu–15Ni–8Sn alloy is discussed, and its

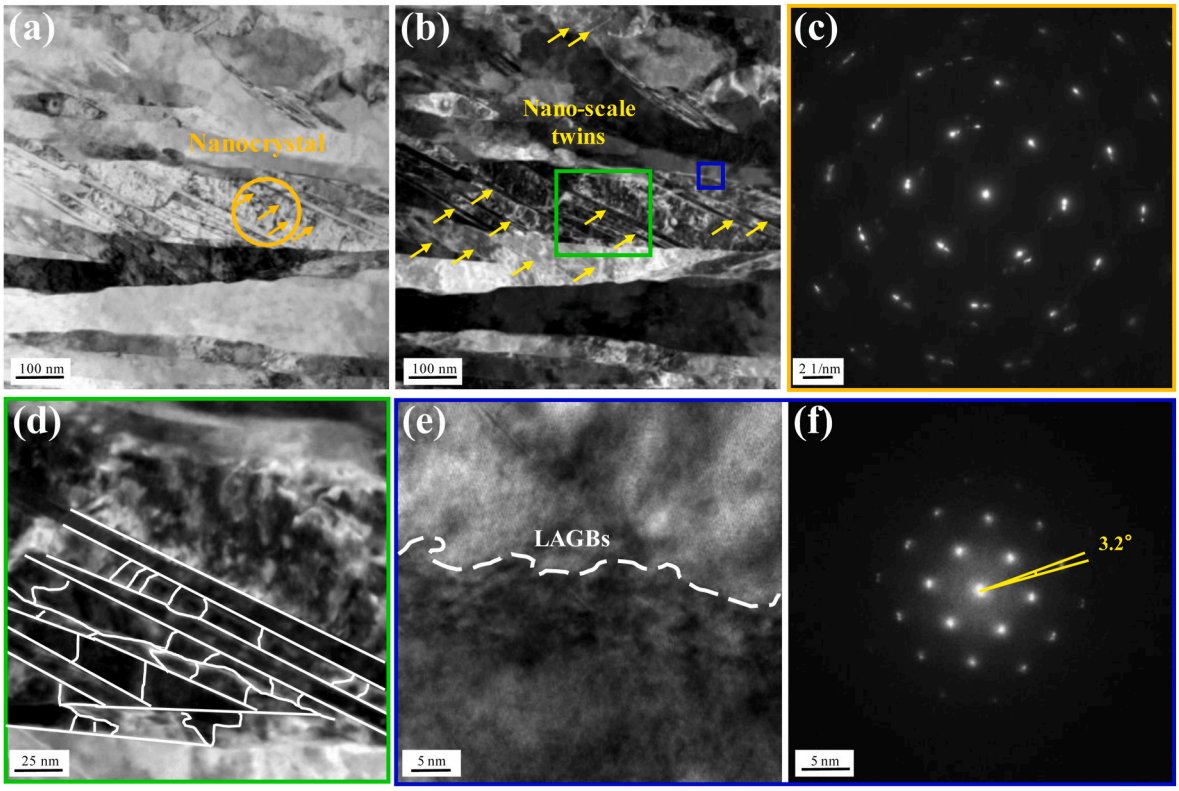

Fig. 23. TEM images of the rotary swaged Cu–15Ni–8Sn alloy with strain ε = 3.9: (a) Bright field image; (b) Dark field image; (c) The orange region in Fig. (a) corresponds to the selected area electron diffraction; (d) An enlarged view of the green boxed area in Fig. (b); (e–f) The blue region in Fig. (b) Corresponds to the high-resolution image and selected area electron diffraction patterns. (For interpretation of the references to color in this figure legend, the reader is referred to the Web version of this article.)

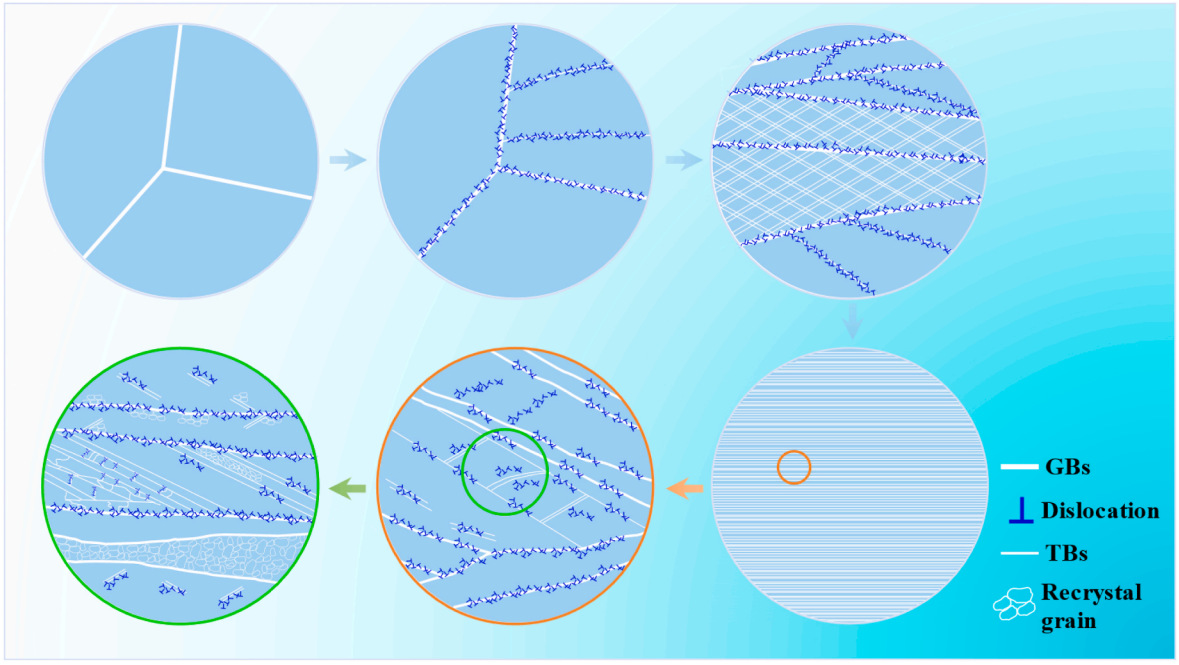

Fig. 24. Schematic diagram of microstructure evolution after rotary swaging of Cu–15Ni–8Sn alloy.

dominant strengthening mechanism is clarified.

The contribution of yield strength of Cu-Ni-Sn alloy comes from solution strengthening (σ_{ss}), grain boundary strengthening (σ_{gb}), dislocation strengthening (σ_d), and precipitation strengthening (σ_p), etc. According to the above results, it is evident no phase transformation occurs after rotary swaging, so the contribution of precipitation strengthening is no longer considered. The formula for calculating the yield strength contribution is as follows [39,40]:

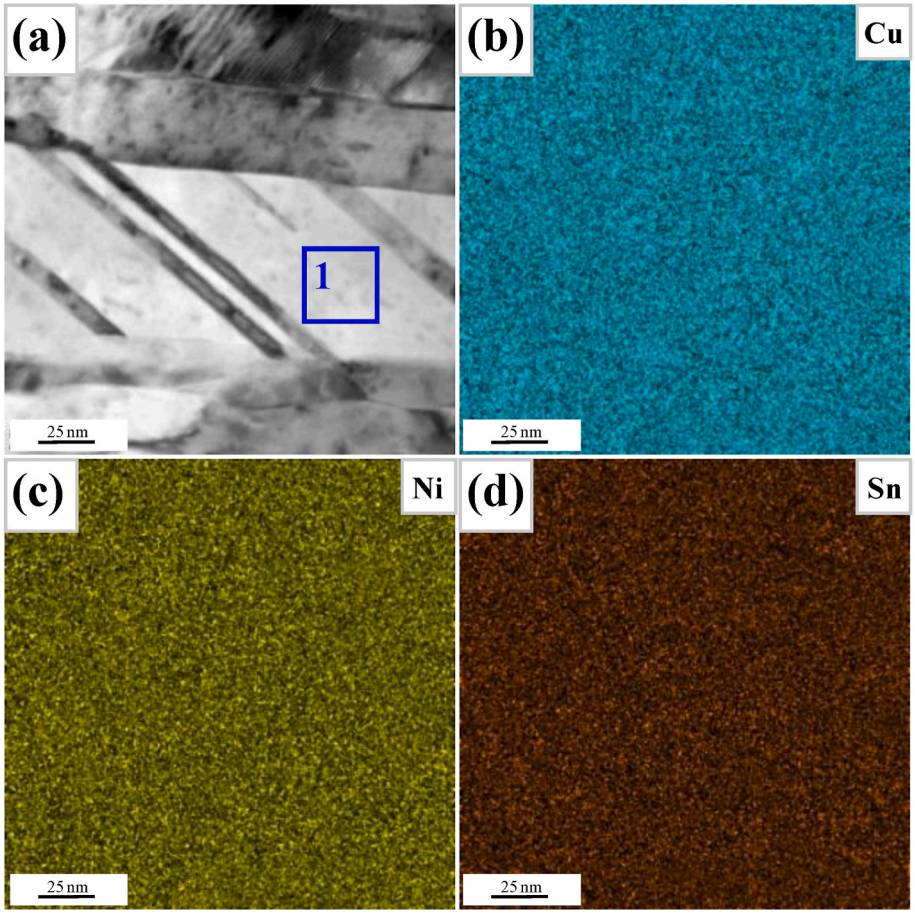

Fig. 25. TEM images of the rotary swaged Cu–15Ni–8Sn alloy with strain ε = 3.9: (a) Bright field image; (b–d) The EDS elemental mapping of Cu, Ni, and Sn.

Table 3
EDS results (at.%) of the corresponding point positions in Fig. 11.

Spectrum	Cu	Ni	Sn
1	80.28	16.24	3.48

$$\sigma_y = \sigma_0 + \sigma_{ss} + \sigma_{gb} + \sigma_d \quad (3)$$

Where σ_y is the yield strength of rotary swaging Cu–15Ni–8Sn alloy with strain ε = 3.9, and σ_0 is the friction stress of pure copper (~52 MPa) [6].

The strength increment of solution strengthening is usually calculated by the following formula [41,42]:

$$\Delta\sigma_{ss} = \frac{MG}{700}\varepsilon_{ss}^{3/2}c^{1/2} \quad (4)$$

Where M is the Taylor impact factor; G is the matrix shear modulus; ε_{ss} is the strain energy caused by the lattice distortion of solute atoms solid in the matrix; c is the concentration of alloy atoms solid in the matrix. In view of the fact that the initial state of Cu–15Ni–8Sn alloy in this paper is a completely supersaturated solid solution (as shown in Fig. 1), when the rotary swaging strain ε = 3.9, there is still no segregation and precipitation (as shown in Fig. 25). The EDS analysis results of blue region 1 in Fig. 25 (a) are shown in Table 3, and the atomic percentages of Ni and Sn in the solid solution in the matrix can be obtained as 16.24 at.% and 3.48 at.%, respectively. Table 4 gives the relevant parameters and calculation results of solution strengthening. Therefore, the solution strengthening increment is 52.58 MPa.

$$\Delta\sigma_{gb} = K_y d_g^{-1/2} \quad (5)$$

Where K_y is the Hall-Petch constant (180 MPa $\mu m^{1/2}$) [22], and d_g is the average grain size (μm). According to the statistics of Fig. 12, the average grain size of the alloy is 1.23 μm. From formula (5), it can be calculated that the grain boundary strengthening increment is 162.30 MPa.

The contribution of the dislocation density to the strength of the alloy can be estimated using the Bailey-Hirsch formula [43]:

$$\Delta\sigma_d = \alpha MGb\rho^{1/2} \quad (6)$$

Where α is the geometric constant (copper alloy α ≈ 0.3); M is the Taylor factor (M ≈ 3.06)[49]; G is the pure copper shear modulus (G = 45.5 GPa); b is the Burgers vector (b = 0.2556 nm); ρ is the dislocation density. According to Fig. 6, when the strain reaches 3.9, the dislocation density of Cu–15Ni–8Sn alloy is 6.97×10^{15} m^{-2}, and the contribution of dislocation strengthening to the alloy strength is 891.32 MPa.

Table 4
Calculation results of related parameters and solution strengthening.

M	G(GPa)	ε_{Ni}	ε_{Sn}	C_{Ni} (at.%)	C_{Sn} (at.%)	$\Delta\sigma_{Ni}$	$\Delta\sigma_{Sn}$	σ_{ss}
3.06	45.5	0.599	0.577	16.24	3.48	36.32	16.26	52.58

The strength increment of grain strengthening is usually expressed by the Hall-Petch formula [43].

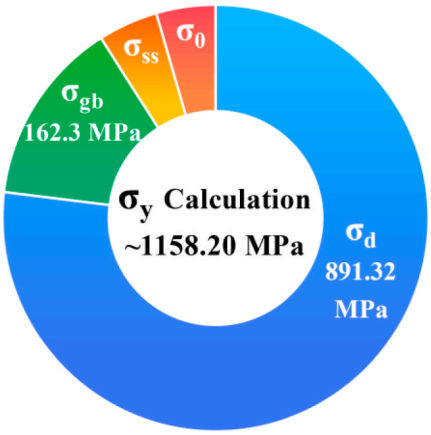

Fig. 26. Strengthening contribution percentage for the yield strength of rotary swaged Cu-15Ni-8Sn alloy with strain ε = 3.9.

It should be further explained that we mentioned in the above analysis that some ultrafine grains are present in the alloy. The presence of ultrafine grains also contributes to the strength. However, this part of ultrafine grains is not ubiquitous, and considering that these ultrafine grains are divided into LAGBs formed by a large number of dislocation plugging, this can be regarded as a dislocation structure. Therefore, the contribution of this part is included in the dislocation enhancement.

In summary, the accumulative contributions of the aforementioned strengthening mechanisms to the yield strength of rotary swaged Cu–15Ni–8Sn alloy at ε = 3.9 total 1158.2 MPa, closely matching the experimentally measured value of 1156 MPa. The relative contribution of each strengthening mechanism to the yield strength is shown in Fig. 26.

5. Conclusion

(1) The evolution of typical microstructure characteristic nodes in Cu–15Ni–8Sn alloy under the large-strain rotary swaging is proved: Dislocation → Cross twins (ε ≥ 1.3) → Layered fine grains (ε ≥ 1.8) → Nanotwins (ε ≥ 2.2) → Nanocrystals (ε ≥ 3.2).
(2) After rotary swaging at large-strain (ε = 3.9), the matrix of the Cu–15Ni–8Sn alloy predominantly exhibits a multiscale microstructure characterized by high-density dislocations and layered fine grains, while nanotwins and nanocrystals are also established locally.
(3) When the accumulative strain ε = 3.9, the tensile strength and yield strength are 1200 MPa and 1156 MPa, which are 1.58 times and 3.22 times higher than those of the undeformed state (ε = 0), respectively. Through the calculation and analysis of strengthening mechanism, the dominant mechanisms of strength improvement are high-density dislocation strengthening and fine-grain strengthening, which contribute approximately 91 % to yield strength.

CRediT authorship contribution statement

Shaodan Yang: Writing – original draft, Visualization, Methodology, Investigation, Funding acquisition, Formal analysis, Data curation. **Yanjun Zhou:** Writing – review & editing, Resources, Project administration, Funding acquisition. **Haoran Wu:** Methodology, Formal analysis, Data curation. **Yunqi Shan:** Supervision, Data curation. **Chenyang Ge:** Methodology. **Juan Du:** Visualization, Funding acquisition. **Lei Zhao:** Writing – review & editing, Data curation. **Ran Yang:** Supervision, Formal analysis. **Zhiyuan Zhu:** Visualization, Methodology. **Xu Gao:** Methodology. **Weiyang Long:** Formal analysis, Data curation, Guoshang Zhang, Writing – review & editing, Project administration, Funding acquisition. **Kai Sun:** Visualization. **Yonghao Zhao:** Writing – review & editing, Resources. **Kexing Song:** Supervision, Resources, Project administration, Funding acquisition.

Declaration of competing interest

The authors declare that they have no known competing financial interests or personal relationships that could have appeared to influence the work reported in this paper.

Acknowledgements

The present work is financially supported by the Henan Academy of Sciences Graduate Innovation Project (24331701), Joint Fund of Henan Province Science and Technology R&D Program (235200810004), Natural Science Foundation of Henan (252300420460), Henan Province Top Talent Training Program Project (244500510020), National Natural Science Foundation of China (52173297), Key Research Project Plan for Higher Education Institutions in Henan Province (24ZX006), National Key R&D Program of China (2021YFB3700700), Henan Provincial Natural Science Foundation Project (No. 242300420030).

Data availability

Data will be made available on request.

References

[1] M. Hu, X. Zhang, C. Liu, X. Gan, Evolution of microstructure and mechanical properties during hot forging and heat treatments of Cu-15Ni-8Sn alloy fabricated by hot isostatic pressing, J. Alloys Compd. 1010 (2025) 178111, https://doi.org/10.1016/j.jallcom.2024.178111.
[2] S. Yang, K. Song, Y. Zhou, R. Yang, Y. Yu, L. Liu, J. Chen, F. Zhou, W. Yang, G. Zhang, J. Du, Research progress on Cu15Ni8Sn alloys: the effect of microalloying and heat treatment on microstructure and properties, Mater 16 (2023) 5913, https://doi.org/10.3390/ma16175913.
[3] F. Zhou, Y. Zhou, K. Song, Y. Zhang, R. Yang, S. Yang, L. Lu, Y. Yu, L. Liu, J. Chen, K. Jiang, W. Yang, The influence of microalloying and preparation process on phase transformation, mechanical properties, and friction/corrosion behavior of Cu–Ni–Sn alloys: a review, J. Mater. Res. Technol. 28 (2024) 951–966, https://doi.org/10.1016/j.jmrt.2023.12.073.
[4] M. Hu, C. Liu, X. Zhang, H. Chen, X. Gan, Deformation mechanisms of the Cu-15Ni-8Sn-0.18Nb alloy in as-quenched and aged conditions, Mater. Sci. Eng. 919 (2025) 147477, https://doi.org/10.1016/j.msea.2024.147477.
[5] Y. Zhou, K. Jiang, S. Yang, R. Yang, P. Yue, F. Zhou, W. Yang, J. Du, H. Guo, X. Peng, J. Yang, K. Song, Synergistic improvement of ultra-high strength and ductility of Cu-15Ni-8Sn alloy induced by multi-pass rotary swaging and aging treatment, J. Alloys Compd. 1012 (2025) 178569, https://doi.org/10.1016/j.jallcom.2025.178569.
[6] S. Yang, Y. Zhou, H. Wu, R. Yang, W. Yang, H. Zhang, R. Shi, F. Zhou, L. Xiao, Z. Zhu, J. Du, K. Song, Ultrahigh strength Cu–15Ni–8Sn alloy: rotary swaging induces twin strengthening and regulates γ (DO_3) phase precipitation, Mater. Sci. Eng. 926 (2025) 147923, https://doi.org/10.1016/j.msea.2025.147923.
[7] P. Zuo, H. Ju, Z. Liu, B. Zhang, Z. Zhang, M. Liu, S. He, X. Luo, Y. Li, B. Peng, J. Wu, X. Li, Influence of heat treatment on the corrosion and tribo-corrosion resistance of LPBF additively manufactured Cu-15Ni-8Sn alloy, Corros. Sci. 250 (2025) 112894, https://doi.org/10.1016/j.corsci.2025.112894.
[8] Z. Guo, J. Jie, J. Liu, S. Yue, S. Liu, T. Li, Effect of cold rolling on aging precipitation behavior and mechanical properties of Cu–15Ni–8Sn alloy, J. Alloys Compd. 848 (2020) 156275, https://doi.org/10.1016/j.jallcom.2020.156275.
[9] J. Kai-Xuan, Z. Yan-Jun, Y. Ran, S. Ke-Xing, L. Ya-Hui, Z. Yan-Min, Y. Shao-Dan, Z. Fei, H. Kuan, L. Dong-Dong, Y. Wen-Hao, Effects of cold deformation and aging on the phase transformation and mechanical properties of a Cu-15Ni-8Sn alloy, Mater. Char. 210 (2024) 113796, https://doi.org/10.1016/j.matchar.2024.113796.
[10] Y. Shi, C. Guo, J. Chen, X. Xiao, H. Huang, B. Yang, Recrystallization behavior and mechanical properties of a Cu–15Ni–8Sn(P) alloy during prior deformation and aging treatment, Mater. Sci. Eng. 826 (2021) 142025, https://doi.org/10.1016/j.msea.2021.142025.
[11] J. Zhang, Z. Wang, S. miao, Y. Zhang, Y. Fu, Y. Dong, S. Liu, J. Jie, Effect of defect strengthening on the mechanical properties of a novel Cu–15Ni–8Sn alloy, Mater. Sci. Eng. 868 (2023) 144777, https://doi.org/10.1016/j.msea.2023.144777.
[12] a M. Wang, H. D Li, Y. B Jiang, M. Fang, Z. Xiao, Y.L. Jia, Microstructure evolution and mechanical properties of Cu–9Ni–6Sn alloy during continuous cold deformation process, Mater. Sci. Eng. 908 (2024) 146950, https://doi.org/10.1016/j.msea.2024.146950;
b K. Zhou, Y. Zhao, Q. Mao, R. Zhang, S. Li, G. Sun, H. Dong, L. Gu, J. Liu,

Simultaneously enhancing strength and ductility of coarse grain Cu–Al alloy via a macro dual-cable structure, Composites, Part B 276 (2024) 111371, https://doi.org/10.1016/j.compositesb.2024.111371.
[13] a H. Kim, J.H. Ahn, S.Z. Han, J. Jo, H. Baik, M. Kim, H.N. Han, Microstructural characterization of cold-drawn Cu–Ni–Si alloy having high strength and high conductivity, J. Alloys Compd. 832 (2020) 155059, https://doi.org/10.1016/j.jallcom.2020.155059;
b Q. Mao, Y. Zhang, Y. Guo, Y. Zhao, Enhanced electrical conductivity and mechanical properties in thermally stable fine-grained copper wire, Communications Materials 2 (2021) 46, https://doi.org/10.1038/s43246-021-00150-1.
[14] a Y.F. Ju, L.C. Zhou, C.J. Shi, R.G. Li, Y. Wang, B. Q Gao, Y.H. Chen, J.Q. Jiang, F. Fang, Planar defect dominated ultra-high strength Cu-Sn-Ni alloy wires with single FCC structure prepared by cold drawing, Mater. Sci. Eng. 927 (2025) 148016, https://doi.org/10.1016/j.msea.2025.148016;
b Y. Wang, J. Zou, L. Sun, Y. Bai, Z. Zhang, J. Cheng, L. Shi, D. Song, Y. Jiang, Z. Zhang, Study on the regulation of microstructure and mechanical properties of Cu–15Sn-0.3Ti alloy by a novel mechanical-heat-electricity synergistic method, Mater. Sci. Eng. 890 (2024) 145928, https://doi.org/10.1016/j.msea.2023.145928.
[15] L. Zhao, L. Chen, B. Luo, Y. Liang, J. Shi, S. Zhang, Z. Lin, P. Shi, T. Zheng, B. Zhou, Y. Guo, Q. Li, C. Liu, Z. Shen, B. Ding, Y. Zhong, Low-dislocation-density ultrafine lamellar structure buffering triples ductility in Cu-8Sn alloy treated by rotary swaging and appropriate annealing, Mater. Sci. Eng. 889 (2024) 145847, https://doi.org/10.1016/j.msea.2023.145847.
[16] Q. Mao, Y. Liu, Y. Zhao, A review on mechanical properties and microstructure of ultrafine grained metals and alloys processed by rotary swaging, J. Alloys Compd. 896 (2022) 163122, https://doi.org/10.1016/j.jallcom.2021.163122.
[17] Q. Mao, L. Wang, J. Nie, Y. Zhao, Enhancing strength and electrical conductivity of Cu–Cr composite wire by two-stage rotary swaging and aging treatments, Composites, Part B 231 (2022) 109567, https://doi.org/10.1016/j.compositesb.2021.109567.
[18] Q. Mao, X. Chen, J. Li, Y. Zhao, Nano-gradient materials prepared by rotary swaging, Nanomaterials 11 (2021) 2223, https://doi.org/10.3390/nano11092223.
[19] S. Xu, Y. Li, M. Zhang, T. Song, H. Ding, S. Jing, Improving strength and elongation combination of Cu–9Ni–6Sn-(0.2Nb) alloys by pre-annealing and aging treatment, Mater. Sci. Eng. 860 (2022) 144221, https://doi.org/10.1016/j.msea.2022.144221.
[20] X. Zhang, J. Zhao, G. Kang, M. Zaiser, Geometrically necessary dislocations and related kinematic hardening in gradient grained materials: a nonlocal crystal plasticity study, Int. J. Plast. 163 (2023) 103553, https://doi.org/10.1016/j.ijplas.2023.103553.
[21] X. Li, Z. Zhang, J. Wang, Deformation twinning in body-centered cubic metals and alloys, Prog. Mater. Sci. 139 (2023) 101160, https://doi.org/10.1016/j.pmatsci.2023.101160.
[22] T. Yeo, N. Shigematsu, T. Katori, Dynamically recrystallized grains identified via the application of Gaussian mixture model to EBSD data, J. Struct. Geol. 167 (2023) 104800, https://doi.org/10.1016/j.jsg.2023.104800.
[23] G. Winther, Slip systems, lattice rotations and dislocation boundaries, Mater. Sci. Eng. 483–484 (2008) 40–46, https://doi.org/10.1016/j.msea.2006.08.138.
[24] R. Su, D. Neffati, Y. Zhang, J. Cho, J. Li, H. Wang, Y. Kulkarni, X. Zhang, The influence of stacking faults on mechanical behavior of advanced materials, Mater. Sci. Eng. 803 (2021) 140696, https://doi.org/10.1016/j.msea.2020.140696.
[25] H. Li, Y. Cui, C. Dan, S. Ma, L. Wang, J. Liu, Y. Li, H. Wang, Z. Chen, Dislocation mechanisms of deformation band formation in precipitation-strengthened alloy studied via in situ micropillar compression, J. Alloys Compd. 1011 (2025) 178407, https://doi.org/10.1016/j.jallcom.2024.178407.
[26] Z.-X. Chen, Y.-J. Song, R.-Z. Li, S.-J. Guo, L. Shi, Z.-R. Yang, X.-M. Xue, T. Zhang, Advances in copper nanocrystals: synthesis, anti-oxidation strategies, and multiple applications, Coord. Chem. Rev. 529 (2025) 216455, https://doi.org/10.1016/j.ccr.2025.216455.
[27] N. Yang, B.-Y. Liu, F. Liu, Z.-W. Shan, The cross-transition of deformation twinning in magnesium, Scripta Mater. 206 (2022) 114231, https://doi.org/10.1016/j.scriptamat.2021.114231.
[28] Y. Cao, Y.B. Wang, X.H. An, X.Z. Liao, M. Kawasaki, S.P. Ringer, T.G. Langdon, Y. T. Zhu, Grain boundary formation by remnant dislocations from the de-twinning of thin nano-twins, Scripta Mater. 100 (2015) 98–101, https://doi.org/10.1016/j.scriptamat.2015.01.001.
[29] B. Anthony, B. Leu, I.J. Beyerlein, V.M. Miller, Deformation twin interactions with grain boundary particles in multi-phase magnesium alloys, Acta Mater. 219 (2021) 117225, https://doi.org/10.1016/j.actamat.2021.117225.
[30] Q. Zhu, L. Kong, H. Lu, Q. Huang, Y. Chen, Y. Liu, W. Yang, Z. Zhang, F. Sansoz, H. Zhou, J. Wang, Revealing extreme twin-boundary shear deformability in metallic nanocrystals, Sci. Adv. 7 (2021) 4758, https://doi.org/10.1126/sciadv.abe4758.
[31] Q. Liu, L. Fang, Z. Xiong, J. Yang, Y. Tan, Y. Liu, Y. Zhang, Q. Tan, C. Hao, L. Cao, J. Li, Z. Gao, The response of dislocations, low angle grain boundaries and high angle grain boundaries at high strain rates, Mater. Sci. Eng. 822 (2021) 141704, https://doi.org/10.1016/j.msea.2021.141704.
[32] I. Dowding, C.A. Schuh, Metals strengthen with increasing temperature at extreme strain rates, Nature 630 (2024) 91–95, https://doi.org/10.1038/s41586-024-07420-1.
[33] Q. Tang, M. Hassani, Quantifying dislocation drag at high strain rates with laser-induced microprojectile impact, Int. J. Plast. 175 (2024) 103924, https://doi.org/10.1016/j.ijplas.2024.103924.
[34] S. Akhondzadeh, M. Kang, R.B. Sills, K.T. Ramesh, W. Cai, Direct comparison between experiments and dislocation dynamics simulations of high rate deformation of single crystal copper, Acta Mater. 250 (2023) 118851, https://doi.org/10.1016/j.actamat.2023.118851.
[35] H. Guo, W. Wu, X. Tan, S. Nie, B. Gan, F. Zhao, N. Jiang, M. Xia, M. He, Ultrahigh strain-rate dynamic recrystallization in high manganese austenitic steels: mechanisms of shear band anisotropy and resistance to localized failure, Eng. Fract. Mech. 325 (2025) 111360, https://doi.org/10.1016/j.engfracmech.2025.111360.
[36] K.K. Alaneme, E.A. Okotete, Recrystallization mechanisms and microstructure development in emerging metallic materials: a review, J. Sci. Adv. Mater. Devices 4 (2019) 19–33, https://doi.org/10.1016/j.jsamd.2018.12.007.
[37] J. Kacher, B.P. Eftink, B. Cui, I.M. Robertson, Dislocation interactions with grain boundaries, Curr. Opin. Solid State Mater. Sci. 18 (2014) 227–243, https://doi.org/10.1016/j.cossms.2014.05.004.
[38] N. Lu, K. Du, L. Lu, H.Q. Ye, Transition of dislocation nucleation induced by local stress concentration in nanotwinned copper, Nat. Commun. 6 (2015) 7648, https://doi.org/10.1038/ncomms8648.
[39] Y. Cao, S.Z. Han, E.-A. Choi, J.H. Ahn, X. Mi, S. Lee, H. Shin, S. Kim, J. Lee, Effect of inclusion on strength and conductivity of Cu-Ni-Si alloys with discontinuous precipitation, J. Alloys Compd. 843 (2020) 156006, https://doi.org/10.1016/j.jallcom.2020.156006.
[40] C. Zhao, Z. Wang, D. Li, D. Pan, B. Lou, Z. Luo, W. Zhang, Optimization of strength and ductility in an as-extruded Cu–15Ni–8Sn alloy by the additions of Si and Ti, J. Alloys Compd. 823 (2020) 153759, https://doi.org/10.1016/j.jallcom.2020.153759.
[41] N. Hansen, Hall–petch relation and boundary strengthening, Scripta Mater. 51 (2004) 801–806, https://doi.org/10.1016/j.scriptamat.2004.06.002.
[42] H. Wen, T.D. Topping, D. Isheim, D.N. Seidman, E.J. Lavernia, Strengthening mechanisms in a high-strength bulk nanostructured Cu–Zn–Al alloy processed via cryomilling and spark plasma sintering, Acta Mater. 61 (2013) 2769–2782, https://doi.org/10.1016/j.actamat.2012.09.036.
[43] W. Luo, L.-J. Peng, X.-J. Mi, H.-F. Xie, Y.-C. Cao, S.-H. Huang, Precipitation evolution and properties of Cu-15Ni-8Sn alloys via Al microalloying during ageing, Rare Met. 43 (2024) 5216–5228, https://doi.org/10.1007/s12598-024-02761-2.